Grant Number: AFOSR-77-3448

STATES OF STRESS AND STRAIN IN

ADHESIVE JOINTS, INCLUDING PHOTOELASTIC IMAGING

OF DEFECTS IN ADHERENDS

J. P./Sargent, T. W./Turner

and K. H. G./Ashbee

H. H. Wills Physics Laboratory, Bristol University, England

November 30th 1979,
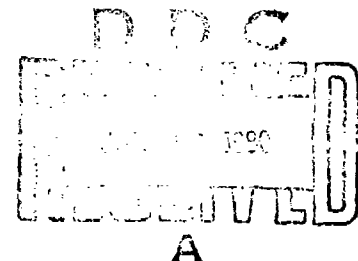
nterim Scientific Report, September 30th 1977 - September 29th 1979

prepared for

UNITED STATES AIR FORCE

AIR FORCE OFFICE OF SCIENTIFIC RESEARCH

Building 410, Bolling Air Force Base, D. C. 20332

and

EUROPEAN OFFICE OF AEROSPACE RESEARCH

AND DEVELOPMENT

223/231 Old Marylebone Road, London NW1 5TH

A

80   1 16 030

REPORT DOCUMENTATION PAGE	READ INSTRUCTIONS BEFORE COMPLETING FORM

1. REPORT NUMBER AFOSR-TR- 79-1359	2. GOVT ACCESSION NO.	3. RECIPIENT'S CATALOG NUMBER

4. TITLE (and Subtitle) STATES OF STRESS AND STRAIN IN ADHESIVE JOINTS, INCLUDING PHOTOELASTIC IMAGING OF DEFECTS IN ADHERENDS	5. TYPE OF REPORT & PERIOD COVERED 30 Sep 77 – 29 Sep 79 INTERIM
	6. PERFORMING ORG. REPORT NUMBER

7. AUTHOR(s) J P SARGENT T W TURNER K H G ASHBEE	8. CONTRACT OR GRANT NUMBER(s) AFOSR 77-3448

9. PERFORMING ORGANIZATION NAME AND ADDRESS UNIVERSITY OF BRISTOL H H WILLS PHYSICS LABORATORY, ROYAL FORT, TYNDALL AVENUE, BRISTOL BS8 1TI ENGLAND	10. PROGRAM ELEMENT, PROJECT, TASK AREA & WORK UNIT NUMBERS 2307B2 61102F

11. CONTROLLING OFFICE NAME AND ADDRESS AIR FORCE OFFICE OF SCIENTIFIC RESEARCH/NA BLDG 410 BOLLING AIR FORCE BASE, D C 20332	12. REPORT DATE Nov 79
	13. NUMBER OF PAGES 50

14. MONITORING AGENCY NAME & ADDRESS(if different from Controlling Office)	15. SECURITY CLASS. (of this report) UNCLASSIFIED
	15a. DECLASSIFICATION/DOWNGRADING SCHEDULE

16. DISTRIBUTION STATEMENT (of this Report)

Approved for public release; distribution unlimited.

17. DISTRIBUTION STATEMENT (of the abstract entered in Block 20, if different from Report)

18. SUPPLEMENTARY NOTES

19. KEY WORDS (Continue on reverse side if necessary and identify by block number)

ADHESIVE	SELF STRESSED FRACTURE MECHANICS
WATER UPTAKE	ULTRASOUND
STRESS ENHANCED MIGRATION OF WATER	
NEWTON'S RINGS	PHOTOELASTIC IMAGING
DIFFUSION	NDE

20. ABSTRACT (Continue on reverse side if necessary and identify by block number)

Water migration across the thin epoxy resin layer in model adhesive joints causes strongly inhomogeneous swelling. The swelling is the principal cause of stress systems which are being examined by analysis of the pattern of Newton's rings formed between a glass cover slip and an optical flat. Enhancement of water migration by normal stresses of the order of a kilobar is reported. The development of a self-stressed fracture mechanics test piece, designed to investigate water uptake by adhesives, is reported. Photoelastic imaging of ultrasonic waves can be utilized to investigate defects in opaque solids. Instead of

DD FORM 1473 EDITION OF 1 NOV 65 IS OBSOLETE
1 JAN 73

using a piezoelectric detector, the reflected sound from a defect is actually observed in a visualizing block of quartz, after propagating from the specimen to the block across an acoustic coupling. Experiments and a computer model are described.

1. Introduction

During the first of the three years of tenure of this contract, water migration across the thin epoxy resin layer in model adhesive joints was studied in detail. Migration rates were measured by monitoring the ingress of the boundary between unswollen (dry) and swollen (wet) resin and were faster than expected for Fickian diffusion. With no evidence to support the presence of channels and hence a capillary explanation for enhanced migration, stress systems were considered to see if a contribution could be attributed to them. Curing is achieved above Tg, the glass transition temperature for the resin. Shrinkage that accompanies curing must therefore be largely relieved by viscoelastic flow. Differential contraction between metal and resin during cooling from the cure temperature is presumably at least partially accommodated by self-adjustment of the glue line thickness, although lateral tensions no doubt remain. A more important source of stress is the resin swelling that accompanies water uptake. This swelling was shown to be strongly inhomogeneous, and is believed to be the principal cause of stress fields and has been under close study from the inception of this project.

The development of a self-stressed fracture mechanics test-piece suitable for water uptake by adhesives was started during the first year and has continued ever since. The original test-piece design was discarded after the first year and has been replaced by a more realistic geometry. This invention is the subject of a US patent application filed by the US Air Force.

The need to generate direct evidence for the presence and locations of defects in our adhesive joints, both those manufactured for swelling studies and those manufactured for fracture mechanics tests, led us into the field of non-destructive evaluation. In
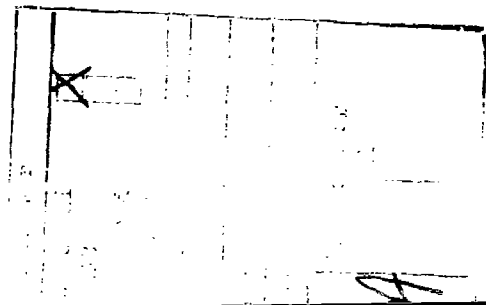
particular work was started on the photoelastic imaging of interference attributable to defects that are generated in ultrasonic wave trains. This followed naturally from previous photoelastic imaging experiments relating to a project on the physical mechanisms responsible for the weathering of epoxy resins and GFR epoxy resins supported by the US Army grant, DA.ERO-76-G-068. Attention was focussed on a computer model which investigates the waves originating from a transducer probe and those waves which emanate from a defect or fault. Experimentation has proceeded in parallel with computation although difficulties have been experienced. In particular, achieving results at frequencies in excess of $10MH_z$ has proved extremely difficult because of inherent increased attenuation, and because resin based specimens (adhesive joints and film composites) tend to dissipate the probing stress waves rapidly, as a result of the close proximity of interfaces which the ultrasound must needs negotiate.

2.   NEWTON'S RINGS EXPERIMENT

2.1. Experimentation

In geometries such as those provided by adhesive joints where, over much of the resin surface, direct access to the environment is restricted, the concentration of diffused water and the swelling associated with it is strongly inhomogeneous. This inhomogeneity is conveniently demonstrated for adhesive films by using a thin and therefore flexible circular glass cover slip bonded to a massive (rigid) adherend such as a microscope slide or a slab of metal.

The experimental arrangement is shown in Figure 1. Light from a mercury vapour discharge lamp is directed through an interference filter, a collimating lens, a half-silvered mirror, an optical flat, and the cover slip. Interference between incident and reflected beams occurs within the variable thickness gap located

between the cover slip and optical flat. The interference pattern is photographed using the light reflected into a 35 mm camera by the half silvered mirror.

The pattern of interference fringes is determined by the geometry of the gap between cover slip and optical flat and, to ensure that changes in the pattern arise only from distortion of the cover slip caused by resin swelling, it is essential that each run be carried out without disturbing the specimen/optical flat assembly. All of the components are set up on an optical bench. Figures 2 and 3 show general views of the ambient temperature and high temperature ($<100^{\circ}$C) apparatus respectively.

It was stated in the Interim Scientific Report, 29th September 1978, that enhancement of fringe contrast as a consequence of multiple beam interference can be obtained by fully silvering the upper surface of the cover slip and partially silvering of the lower surface of the optical flat. A range of reflective coatings has now been evaluated from which it is evident that a chromium layer is most effective, having sufficient water resistance to withstand a full length boiling water test. The main disadvantages of a chromium layer are that it obscures direct observations of the adhesive and is difficult to remove should it need renewing. An alternative and very successful method for securing multiple beam interference and hence for improving fringe definition has been realised by using a wedge shaped optical flat. With a wedge angle of 4° the image of the Newton's rings does not coincide with reflections from other glass or water surfaces. The wedge is made from flint glass with refractive index 1.65 and has been incorporated into a mark II version of the hot water apparatus designed to permit undisturbed tests at any fixed temperature between ambient and 100°C. This is shown in

Figure 4.

2.2   Results and Discussion.

The first long term test was made at room temperature on a
joint between a cover slip and cleaned, but not anodised. S1C
aluminium. A general purpose epoxy resin containing entrapped air
bubbles was used as adhesive. Hereafter, this adhesive will be
referred to as adhesive A. Its full identity, including hardener and
accelerator, and the curing schedule used for it are given in Table 1.

Later tests were carried out on joints between a cover slip
and substrates of both stainless steel and anodized titanium using
the commercially available adhesive film system designated B in
Table 1. All metal surfaces were cleaned and, where applicable,
treated in accordance with commercially accepted practice. The
metal based specimens were supplied by Westland Helicopters Ltd
in the form of cleaned and pre-primed coupon specimens.

For tests employing the adhesive film systems designated
C and D in Table 1 both adherends were glass. Preparation of the
glass cover slip surfaces is less well standardised. The fundamen-
tal problem is removal of oxides of low surface energy. Chemical
attack by the common oxidising agents, e.g. nitric acid and hydro-
gen peroxide certainly remove a large fraction of these oxides. So
too does exposure to the oxidising region of a naked flame. Sand
blasting in order to roughen the surface and promote mechanical
linkages, and application of coupling agents (silanes) have also
been recommended. However, no combination of these treatments
has yet produced a joint which, when it eventually debonds after
prolonged exposure to water in the absence of externally applied
stress, leaves fracture surfaces which do not include large areas
of glass/adhesive interface.

Table 1

Adhesives and Curing Schedules

Resin system	Proportions p.b.w.	Gel	Cure
A Ciba Geigy			
MY 750 (Diglycidyl ether of bisphenol A)	100	2 hours at 100°C	4 hours at 150°C
HY 917 (Methyl tetrahydro-phthalic anhydride)	85		
DY 062 (Triamyl ammonium phenate)	2		
B Bloomingdale			
FM 1000 (Nylon modified epoxy film)			1 hour at 170°C
BR 1009/49 (Phenolic primer)		2 hours at 20°C	1 hour at 70°C
C Ciba-Geigy (modified epoxy film) Redux 312/5			½ hour at 120°C
D Bloomingdale FM 73M (modified epoxy film)			1 hour at 120°C

In joints manufactured using liquid resin, a reproducible glue line thickness was achieved by simply allowing the cover slip to sink under its own weight. In joints made using solid adhesive film, the glue line thickness was controlled by clamping during the cure process.

Adjacent rings of the same colour (black or white) are loci of points for which the optical path length, in the space between cover slip and optical flat, differs by one wavelength. By the same token, a displacement in the pattern of Newton's rings by an amount equal to one ring width corresponds to a change in path length equal to one wavelength. By observing changes in the number of rings between fixed markers, such as entrapped air bubbles, displacements normal to the joint during water uptake can be measured to an accuracy of $\lambda/4$. If required, displacements which are at least as small as $\lambda/10$ can be measured by superimposition of images in order to create Moiré patterns.

The water concentration, and hence the swelling associated with water uptake, eventually saturates and thereafter a shoulder separating fully saturated from less than fully saturated resin, progressively moves inwards from the rim of the joint. This is shown schematically in Figure 5c. Figure 6 shows a sequence of images obtained, showing the development of swelling in a joint manufactured between anodized titanium and a glass cover slip using adhesive B and immersed in distilled water at approximately $80^{\circ}C$.

To maintain contact with the outer ring of uniformly swollen adhesive (Figure 5c), the adherends would each need to bend with curvature that is opposite to that inside the shoulder. Failure to adopt such "S" wise bending manifests itself as an interfacial crack, the occurrence of which is revealed as patches of bright contrast at

the rim in Figure 6.

The positions of well defined points in the patterns of Newton's rings may be measured as functions of time. Figure 7 shows a plot of the shoulder defining the extent of water saturation, and of the crack edge as functions of $(time)^{\frac{1}{2}}$ for an aluminium joint manufactured with adhesive A and immersed in distilled water at $20^{\circ}C$.

Figure 8 shows a plot of the shoulder defining the extent of water ingress from the experiment reported in Figure 6.

Figure 9 shows a similar plot for a specimen manufactured using adhesive B but with a stainless steel substrate and for an immersion water temperature of $80^{\circ}C$. From the marked similarity in the results for anodized titanium and stainless steel it is concluded that the deformation is wholly within the adhesive and is independent of the adherend. Moiré patterns, generated by superimposition of interference patterns before and after swelling were used to obtain the data in Figure 10. These specimens were manufactured from adhesives C and D and measurements were made at a range of temperatures between ambient and $100^{\circ}C$.

If migration of water occurs at low water concentrations and is governed by Ficks' laws, plots of migration distance as a function of $(time)^{\frac{1}{2}}$ should approximate to straight lines. The data points for specimens manufactured with adhesives A and B certainly do not approximate to straight lines. However those manufactured with adhesives C and D and which were studied using the more precise Moiré measuring technique do suggest Fickian behaviour although the slopes of the graphs indicate activation energies that are much higher than normally expected for epoxy resins.

3.   SELF STRESSED FRACTURE MECHANICS TEST-PIECE

3.1.   The plane elastic problem.

The disc consists of a circle of aluminium which in plane polar coordinates is defined by the relations $0 \leqslant r \leqslant a$ and $0 \leqslant \theta \leqslant 2\pi$. It is stressed by removing a sector $0 \leqslant r \leqslant a$, $2\pi - \Omega \leqslant \theta \leqslant 2\pi$ and making an adhesive joint when the gap has been closed. Assuming that plane stress conditions are met, it is necessary to calculate the stress intensity factor, K_I, and the formation energy, W, for the crack $c \leqslant r \leqslant a$, $\theta = 0$. This has been done by superimposing the solutions of the resulting stress with those of K_I and W for a traction free circumference and a symmetrical pressure loading.

The Airy function given by Michell (1899), Eshelby (1966),

$$\psi(r, \theta) = a_o + b_o \ln r + c_o r^2 + d_o r^2 \ln r \qquad 3.1$$

may be used to find the stress and displacement fields:

$$\sigma_{rr}(r, \theta) = b_o r^{-2} + 2 c_o + d_o (1 + 2 \ln r) \qquad 3.2$$

$$\sigma_{r\theta}(r, \theta) = 0 \qquad 3.3$$

$$\sigma_{\theta\theta}(r, \theta) = -b_o r^{-2} + 2c_o + d_o (3 + 2 \ln r) \qquad 3.4$$

$$u_r(r, \theta) = E^{-1} \left\{ -b_o(1+\nu)r^{-1} + 2c_o(1-\nu)r + 2d_o(1-\nu)r \ln r - d_o(1+\nu)r \right\} \qquad 3.5$$

and

$$u_\theta(r, \theta) = 4 E^{-1} d_o r\theta \qquad 3.6$$

Since the solution is required to satisfy the conditions

Mitchell, J.H. 1899 Proc. Lond. Math. Soc. 31, 100.
Eshelby, J.D. 1966 Brit. J. Appl. Phys. 17, 1131-1135.

(i) $\sigma_{rr}(a, \theta) = \sigma_{r\theta}(a, \theta) = 0$, $0 \leqslant \theta \leqslant 2\pi$, (ii) $u_\theta(r, 2\pi) = r^{\frac{1}{2}}$ and

(iii) u_r and u_θ are bounded at $r = 0$, we see that $b_o = 0$, $d_o = E\lambda/8\pi$

and $c_o = -(E\lambda/8\pi) \ln (a \sqrt{e})$. Therefore,

$$\psi(r, \theta) = \frac{E\lambda}{8\pi} \quad r^2 \ln \quad (r / a \sqrt{e}) \qquad 3.7$$

and

$$\sigma_{\theta\theta}(r, 0) = \frac{E\Omega}{4\pi} \left\{ 1 + \ln (r / a) \right\} \qquad 3.8$$

It follows that we may write $\sigma(r) = p_o f(r/a)$ where

$$p_o = E\lambda/4\pi \text{ and } f(\rho) = 1 + \ln \rho.$$

To find K_I and W the dimensionless quantities $\rho = r/a$ (already introduced) may be used

$$s_{\rho\rho}(\rho, \theta) = \frac{\sigma_{rr}(r, \theta)}{p_o}, \quad s_{\rho\theta}(\rho, \theta) = \frac{\sigma_{r\theta}(r, \theta)}{p_o}, \quad s_{\theta\theta}(\rho, \theta) = \frac{\sigma_{\theta\theta}(r, \theta)}{p_o} \qquad 3.9$$

$$u(\rho, \theta) = \frac{E u_r(r, \theta)}{p_o(1+\nu)a} \quad \text{and} \quad v(\rho, \theta) = \frac{E u_\theta(r, \theta)}{p_o(1+\nu)a}$$

then, by making use of a symmetry argument, it is easily shown that the problem to find K_I and W may be stated as follows:

Solve the dimensionless, plane stress equations of elasticity in the semi-disc $0 \leqslant \rho \leqslant 1$, $0 \leqslant \theta \leqslant \pi$ subject to the conditions

(i)   The stresses and displacements are bounded at $r = 0$.

(ii) $s_{\rho\rho}(1,\theta) = s_{\rho\theta}(1,\theta) = 0$, $0 \leqslant \theta \leqslant \pi$

(iii) $s_{\rho\theta}(\rho,0) = s_{\rho\theta}(\rho,\pi) = 0$, $0 \leqslant \rho \leqslant 1$

(iv) $v(\rho,\pi) = 0$, $0 \leqslant \rho \leqslant 1$

(v) $v(\rho,0) = 0$, $0 \leqslant \rho \leqslant c$

(vi) $s_{\theta\theta}(\rho,0) = -(1 + \log \rho)$, $c \leqslant \rho \leqslant 1$

(vii) $\displaystyle\lim_{\rho \to 1-} \frac{\partial v(\rho,0)}{\partial \rho} < \infty$

By slightly modifying the results in section 2 of Tweed and Rooke (1973) it can be shown that there is a solution of the equations of elasticity, in the given region, which satisfies the conditions (i) through (v) and is such that

$$s_{\theta\theta}(\rho,0) = \frac{1}{\pi} \int_c^1 \frac{P(t)\ M(\rho,t)dt}{\sqrt{[(1-t)(t-c)]}} \quad , \quad 0 \leqslant \rho \leqslant 1 \qquad 3.10$$

and

$$v(\rho,0) = \frac{2}{1+\nu} \int_c^\rho \frac{P(t)\ dt}{\sqrt{[(1-t)(t-c)]}} \quad , \quad c \leqslant \rho \leqslant 1 \qquad 3.11$$

where $P(t)$ is an arbitrary function of t

and

$$M(\rho,t) = \frac{1}{t-\rho} + \frac{(t^2-1)^2}{t(1-\rho t)^3} + \frac{t(t^2-1)}{(1-\rho t)^2} - \frac{t}{(1-\rho t)} + t - \frac{1}{t} \qquad 3.12$$

It follows that conditions (vi) and (vii) will be satisfied also if $P(t)$ is a solution of the singular integral equation

Tweed J. and Rooke D.P. 1973 Int. J. Engng. Sci. 11, 65-73.

$$\frac{1}{\pi} \int_c^1 \frac{P(t)\, M(\rho, t)\, dt}{\sqrt{\left[(1-t)(t-c)\right]}} = -(1 + \log \rho), \quad c < \rho < 1 \tag{3.13}$$

with subsidiary condition

$$P(1) = 0 \tag{3.14}$$

The stress intensity factor K_I and the crack formation energy W are defined by the equations

$$K_I = \lim_{r \to ac+} \sqrt{2\pi(r - ac)} \; \frac{E}{2} \frac{\partial u_\theta(r, 0)}{\partial r} \tag{3.15}$$

and

$$W = \int_{ac}^a p_0 \left[1 + \log(r/a)\right] u_\theta(r, 0)\, dr \tag{3.16}$$

respectively. Therefore, by 3.10 and 3.11, we see that

$$K_I = p_0 \sqrt{\frac{2\pi a}{1 - c}} \; P(c) , \tag{3.17}$$

and

$$W = -\frac{2 p_0^2 a^2}{E} \int_c^1 \frac{t\, P(t) \log t}{\sqrt{\left[(1-t)(t-c)\right]}}\, dt \tag{3.18}$$

Let K_0 and W_0 be the stress intensity factor and formation energy respectively of a crack of length $2(a - ac)$ in an infinite elastic solid, when the crack is opened by a uniform pressure p_0, then after Sneddon and Lowengrub (1969)

Sneddon I. N. and Lowengrub M. 1969 Crack Problems in the Classical Theory of Elasticity   Wiley J. and Sons N. Y.

$$K_o = p_o \sqrt{\pi a (1-c)} \qquad \qquad 3.19$$

and

$$W_o = \frac{\pi p_o^2 a^2 (1-c)^2}{E} \qquad \qquad 3.20$$

Therefore

$$\frac{K_I}{K_o} = \frac{\sqrt{2}}{1-c} P(c) \qquad . \qquad \qquad 3.21$$

and

$$\frac{W}{W_o} = -\frac{2}{\pi(1-c)^2} \int_c^1 \frac{t \, P(t) \, \log t}{\sqrt{[(1-t)(t-c)]}} \, dt \qquad 3.22$$

Also of interest is the strain energy release rate $\mathcal{G}(\ell)$ which is defined by

$$\mathcal{G}(\ell) = \frac{\partial W}{\partial \ell} = \frac{1}{E} K_I^2 \qquad \qquad 3.23$$

where $\ell = a(1-c)$ is the crack length.

If we define

$$\mathcal{G}_o(\ell) = \frac{1}{E} K_o^2 = \frac{p_o^2 \pi a (1-c)}{E} \qquad . \qquad \qquad 3.24$$

then

$$\frac{\mathcal{G}}{\mathcal{G}_o} = \frac{K_I^2}{K_o^2} = \frac{2}{(1-c)^2} P^2(c) \qquad \qquad 3.25$$

Numerical solutions to equation 3.5 are found by the Gauss-Chebyshev quadrature technique, Erdogan and Gupta (1972), and the ratio K_I/K_O using Chebyshev-Lagrange interpolation. The Gaussian quadrature formula is used to determine W/W_O.

3.2 Experimentation

Preliminary experiments were carried out using $3''(7.6$ cm) diameter SIC aluminium discs, $1/16''$ (0.16 cm) thick with a 5° sector cut out and a $\frac{1}{2}''$ (1.27 cm) diameter central hole. The hole is helpful during manufacture and reduces pinching on disc closure. However, it was found that taking typical values for the physical properties of NSI (C) aluminium, significant areas of the disc are stressed to levels above the elastic limit and even above the UTS. This serious objection to the initial design was aggravated by a buckling factor. Mitchell and Head (1961) calculated that a disclinated plate will buckle if the angle exceeds, Ω buckle $\geqslant 13$ (thickness/radius)^2. For the original disc, $\Omega_b = 1^O 20'$ and would deform to a cone.

The thickness of the disc was increased to $3/16''$ (0.48 cm) which ensures that closure after removal of a 5° sector can be achieved without buckling. This decision to increase the thickness rather than reduce the sector angle was taken because of difficulties associated with manufacturing and gluing the disc. With the 5° sector cut out, gap closure with a custom built chain wrench, was found to cause the centre to close too quickly. Parallel sided gaps were examined with gaps varying from $0.098''$ (2.5 mm) to $0.019''$ (0.5 mm). With gap sizes greater than $0.046''$ (1.15 mm) the rims of the disc pinched thereby preventing closure. Below $0.039''$ (1 mm) the pinching effect while still present, was less noticeable. The most

Erdogan F. and Gupta, G.D. 1972 Q. Appl. Math. 29, 523.

Mitchell and Head, (1961) J. Mech. Phys. Solids, 9, 131.

uniform closure was achieved with a wedge shaped cut out. The dimensions were calculated from empirical data collected from repeated opening and closing of the 0.039" (1 mm) and 0.019" (.5 mm) parallel sided gaps. The optimum wedge dimensions were found to be 0.046" (1.2 mm) at the specimen periphery reducing to 0.032" (0.8 mm) at the central hole. Some plastic deformation was observed to take place on closure, thus demonstrating that the maximum amount of elastic energy was being stored in the discs, as required.

A thorough cleansing schedule was devised to remove all atmospheric corrosion and included anodizing in phosphoric acid. Adhesive joints were made within two hours and therefore before the onset of further attack by the atmosphere.

To date three proprietary adhesive resin films have been used FM73M, BSL 312/5, and DLS 468/DLS 476. Two restraining plates were used to maintain discs flat during the closing operation and, to obtain standardisation, a torque wrench set at 16 ft.-lb. was employed. On closure, the restraining plates were removed and the clamped disc was placed in an oven for curing. Strict adherence to the manufacturer's data sheets was maintained for the cure times and temperatures. The disc was allowed to cool in a desiccator before releasing the clamp with the disc once again sandwiched between the restraining plates.

Starter cracks were not artificially introduced. Instead, each specimen was boiled in distilled water until, as a consequence of resin degradation, a crack had nucleated. Thereafter, the crack length was measured as a function of time of immersion in boiling water. Since the crack length measured each side of the disc invariably gave two values, the

average measurement was taken as the true value. Attempts to introduce starter cracks by making a small cut or by immersing in liquid nitrogen in order to shrink the aluminium and hence increase the stress field, proved unsatisfactory.

A few experiments were performed using a perspex disc of similar dimensions to the aluminium specimens. The object here was to use a photoelastic method to study the stress field during crack growth. Crack initiation proved difficult and satisfactory monitoring of the stress field during propagation was not achieved.

3.3 Results and Discussion

On release of the chain-wrench clamp from around the stressed disc, crack lengths vary according to the epoxy resin adhesive formulation used to make the joint. The crack always propagates the full glue-line length ($l/a = 1$) for resin Redux 312/5, whereas for FM 73M no crack is present in the joint ($l/a = 0$). The l/a values obtained for DLS 468/DLS 476 are 0, 0, 0, 0.40 and 0.82.

Correlation of crack length with independently measured values of G_{IC} is required in order to generate calibration curves for a given geometry of self stressed disc. Available G_{IC} data for the dry adhesives show variations, e.g. FM73M has values of 2.38 kJ/M^2 and 3.67kJ/M^2 for two different batches. Redux 312/5 and DLS 468/DLS 476 both have G_{IC} values of 2.8 kJ/M^2. Using as calibration points, the G_{IC} values for dry FM73M and Redux 312/5 and the stable crack lengths measured after mechanically introducing starter cracks, two values of l/a measured for DLS 468/DLS 476 indicate that $(G_{IC})_{max}$ is 3.65 ± 0.55 kJ/M^2.

Conflict evidently exists between the published data and the results

obtained here, with DLS 468/DLS 476 our self-stressed discs crack partially or not at all. With Redux 312/5, the bonds crack over the full length of the glue line. With FM73M no cracks are found suggesting that $\mathcal{G}_{IC}$ is greater than 2.8 kJ/M^2. With a view to clearing up this dilemma, independent measurements of $\mathcal{G}_{IC}$ on the particular batches of adhesive films used here are being made at the University of Cambridge.

Results presenting the variation of $\mathcal{G}_{IC}$, expressed as a fraction of $(\mathcal{G}_{IC})_{max}$, with water uptake by FM73M are shown in Figures 11 to 14. The specimens were immersed in boiling distilled water. The time for the starter crack to appear varied from 5 to 130 mins. Examination of the joints after total failure show that propagation of the cracks occur through the resin and definitely not at the resin/aluminium interface.

4.   PHOTOELASTIC IMAGING OF DEFECTS

Andrews and Wallis (1977) were first to demonstrate that a light emitting diode (LED) can be used to illuminate the stress waves travelling in a visualizing block when viewed through crossed polars. The method was applied to the detection of defects in opaque solids by Hardy, Turner and Ashbee (1978). There is a strong reflected component, mode converted, from a defect which can be observed some distance from the flaw, after the stress wave has travelled from the specimen into the transparent block. This wave interacts with direct waves from the transducer to give interference patterns for which a computer model has been devised by Kitson, Low and Turner (1979). All the longitudinal and shear waves emanating from the transducer, the interface and the defect, with and without mode conversion, are investigated.

Andrews and Wallis, 1977, J. Phys. E. 10, 95.
Hardy, Turner and Ashbee, 1978, Metal Science, 12, 406.
Kitson, Low and Turner (1979) 'Ultrasonics International 79' Graz, Austria.

4.1   Computer Model

Figure 15 shows the representation of the model, with a series of radiating point sources depicting the transducer. An array of points $P(x,y)$ forms the visualized zone and was originally set at 31 x 31 to conform with computer graphics. It is assumed that the defect is perfectly round, that longitudinal (L) and shear (S) waves emanate from the transducer point sources, and that on reflection and refraction both mode converted and unconverted waves emerge. The following relationships hold:

$$\frac{\sin \beta}{V_L} = \frac{\sin \alpha}{V_S} \quad , \qquad \frac{\sin \gamma}{V_S} = \frac{\sin \delta}{U_S}$$

where V_L and V_S are the velocities in the specimen and U_S the shear velocity in the visualizing quartz. Note that the subscripts are interchangeable for the incident shear wave reflected as longitudinal and for a refracted longitudinal wave. Relative intensities may be evaluated using the Zoeppritz equations and an attenuation factor of $1/\sqrt{x}$ is included for the wave amplitude as it travels away from the source. Hence we may find the exact path which any particular ray travels together with its amplitude at any point. Each flash of the LED is represented by a sine wave, singly for single flash and several cycles for multi-flash.

The complete picture is built up as follows: Each type of wave (longitudinal/shear (LS), long/long/shear (LLS), etc.) is considered in turn for each transducer point source. The program calculates (i) the path between the transducer point and a point in the rectangular visualized array (subject to the path being possible, (ii) when the sound pulse arrives at the visualizing point, and (iii) the amplitude. The amplitude is then multiplied

by the value of the illumination waveform at that specific time, and repeated for all the points in the rectangle. Results for all the transducer elements are superimposed, and finally the whole process repeated for each wavetype in order to simulate the complete interference pattern. The final array is normalized to give the negative or compressive regions the lighter shades of the computer simulation and the positive or tensile regions the darker areas: a normalization analogous to the quarter wave plate.

Two main calculation procedures are used in the program, REFPATH and DIRCALC. REFPATH, the flow diagram is shown in Figure 16, deals with the patterns resulting from wavetypes which are reflected from the defect, whilst DIRCALC handles those direct from the transducer. Any wavetypes can be included, but it is found experimentally that many are of little importance and only LLS, LS, and SSS need to be considered. It should be remembered here that the experimental arrangement of the photoelastic method helps enormously to reduce the number of wavetypes which contribute to the visualization. In the direction of principal stress, i.e. the direction of the stress wave propagation, 45° to the polar axes, only longitudinal waves are visualized, and at 45° to this direction, along the polar axes, only transverse waves can be seen. It is in this direction, along the polar axes, that we are primarily concerned as it is here that most information is displayed.

The first attempts to display the visualized array by computer graphics took advantage of SYMAP[*] and then SYMVU was employed to give a topographical representation of the data. The former program had the advantage that direct comparisons could be made of the photographic results, but suffered from having only ten levels of shading, whereas the latter shows the

*SYMAP is a computer program for producing maps which graphically depict spacially disposed quantitative and qualitative information. SYMAP was designed and developed by the Laboratory for Computer Graphics at Harvard University, U.S.A.

dislocations very well. Figure 17 shows the contour map where the maximum pressure is represented by a height of 3", with a minimum of 0". The viewing point is at an altitude of 30" with an azimuth of 335°. Dislocations in this context refer to the line of discontinuities in wavefronts which line runs in the direction of the stress propagation. A new program was written therefore, following the principles of SYMAP, but with facility for 100 shadings. Some time was spent experimenting with different overprinted characters in order to get a set of evenly varying shades. It was found that a subroutine designed to interpolate the brightness between the array points gave a smoother picture when the visualization density map was plotted on the line printer.

4.2   Visualized sound experiments

Figure 18 shows a schematic diagram of the apparatus. The LED sends a single pulse (single flash) or flashes a number of times in synchronisation with the ultrasonic frequency (multi-flash) to illuminate the stress field in the quartz visualizing block. The birefringence exhibited by quartz when it is stressed, results in a small component of light being propagated perpendicular to the axis of the polarizer to give elliptically polarised light. This contrasts with transmission of the illuminating pulses through unstressed regions of the quartz since here the light remains plane polarised. The analyser, set at 90° to the polarizer, permits transmission of the small component only so that the stressed regions are revealed as bright fringes. Bright fringes arise in both tensile and compressive regions, and, by suitably setting the quarter wave plate, all the light from the most highly compressed region can be eliminated. Thus some light can be seen for unstressed regions

with the tensile areas brighter still, the whole picture being built up strobo-scopically at repetition rates up to 3 kHz. Full details of the experimental approach are given in Hardy, Turner and Ashbee (1978).

The experiments which have been carried out in parallel with the computer modelling have been mostly single flash, i.e. a single LED pulse for illumination. Single flash images are difficult to record because they are so dim, but it is necessary to identify the different wavetypes. A series of experiments were conducted with no specimen in place in order to investigate the transducer for accurate computer modelling. For these, three flashes were used. As the shear waves travel more slowly than the longitudinal waves, the shear fringes are closer together: a fact which with their position simplifies the identification of any particular wave. To investigate the transducer beam, a series of photographs was taken varying the polar axes, thus compensating for the angular sensitivity of the optical arrangement. The angular spread of the beam was found to be approximately 90°.

A number of different transducers have been tried including two commercial designs, but the best results have been obtained with a transducer designed and built in the laboratory. It consists essentially of a brass plate 0.9" (2.2 cm) diameter and $5\lambda/4$ thick on to which a 0.4" (1.0 cm) diameter piezo-electric disc is soldered. However, the image is still complicated by secondary waves arising from reflections within the brass and disc.

After the initial experiments it appeared that two wavetypes were contributing to interference patterns seen in the visualized region. Firstly, the wave reflected from the defect. This is mode converted but crosses the interface between specimen and visualizing block without a further conversion (LSS). Secondly, the direct wave originating as shear at the transducer and

again crossing the interface without mode conversion (SS). The experiments show, however, that the prominent shear waves leave the specimen/quartz interface at roughly the same time as the primary longitudinals. To investigate this further, the positions of the primary longitudinal and shear waves were plotted for a series of different delay times. Different specimen thicknesses were used for the measurements as well as readings taken without a specimen. The results shown in Figure 19 strongly suggest that the shear waves arise by way of mode conversion at the interface, having crossed the specimen as longitudinal waves. Shear waves generated from the transducer are apparently unimportant. Different effects of the quarter wave plate on the two wavetypes account for the incorrect positioning of the specimen/quartz interface in that Figure.

To establish a baseline from which to judge images from resin specimens a range of steel specimens have been produced with thicknesses up to $1\frac{1}{4}$" (31.2 mm) each containing a transverse hole 'defect' having diameters in the range 0.04" (1 mm) to 0.4" (10 mm). A 35 mm Nikon F2 photomic camera is used to record the results with an eight minute exposure on ASA 400 film for single flash at different delay times.

The delay time is measured from the original ultrasonic pulse to the LED flash, and is the time taken for the sound to travel from the transducer to the visualized position. The TTL control enables this to be accurately measured, since the delay monostable and thyrister fired ultrasonic wave are triggered by the same pulse. A digital readout of the delay is used which can be checked against the time base of the oscilloscope.

4.3 Results and Discussion

The results are presented in a graphical form which show both experimental position and the computer simulation. Figures 20 and 21 show the results for two delays, 8.8 and 13.4 μs respectively for steel specimens. The dotted lines give the position of the computer prediction and the hard lines have been traced from the photograph. They show that the program correctly predicts the wavefront spread for both the LSS and LS waves. It is the former which represents 'information' from the defect. Differences in the lengths of the wavefronts can be attributed to the differences in the transmission coefficients. The latter are complicated by the acoustic coupling at the specimen/quartz interface by a thin film of water. Broadening of the lower LS wave is caused by the superposition of the LLS wave i.e. the reflection from the hole without mode conversion.

The experimental delay times against the theoretical time required to align the LS waves is shown in Figure 22. The gradient of unity within 3% demonstrates further that the program correctly predicts the LS position.

A sequence of tests was undertaken with thicker specimens, $1\frac{1}{4}''$ (31.2 mm) containing a hole 0.3" (8 mm) diameter, where the distance between the hole centre and the transducer, A, was varied. Figures 23, 24 and 25 give the results for A = 0.27" (7 mm), 0.61" (15.6 mm) and 0.95" (24.2 mm) respectively.

The above results refer to single flash which was regarded as the best approach for wave identification, whereas the original approach began with multiflash. More information is carried in the multiflash pictures as the close up of the interference patterns from a 0.04" (1 mm) radius 'defect' shows in Figure 26. The multiflash simulation of Figure 27 illustrates the

interaction of the LS wave and the LSS wave reflected from a hole of 0.04" (1 mm) radius.

In composite materials it has been possible to calculate both longitudinal and shear wave velocities by measuring the delays across a known specimen thickness. Velocity variations have been detected during water uptake and are attributed to resin plastication and to post curing. Experiments on composite laminates containing holes have been less successful. Attenuation of the wavetypes is more marked, and the shear wave rapidly loses energy as it proceeds across a series of interfaces. The problem is aggravated by higher frequencies, resolution of the fringes being impossible at frequencies in excess of ~ 10 MHz.
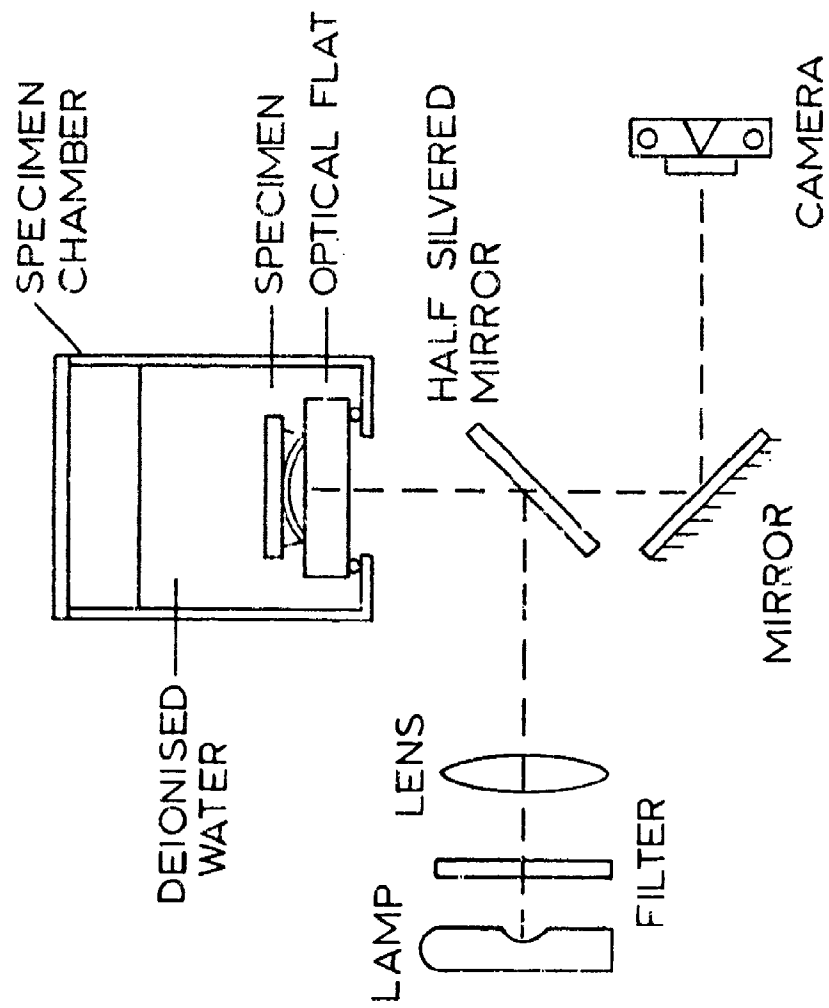
Figure 1   Experimental arrangement of Newton's rings apparatus
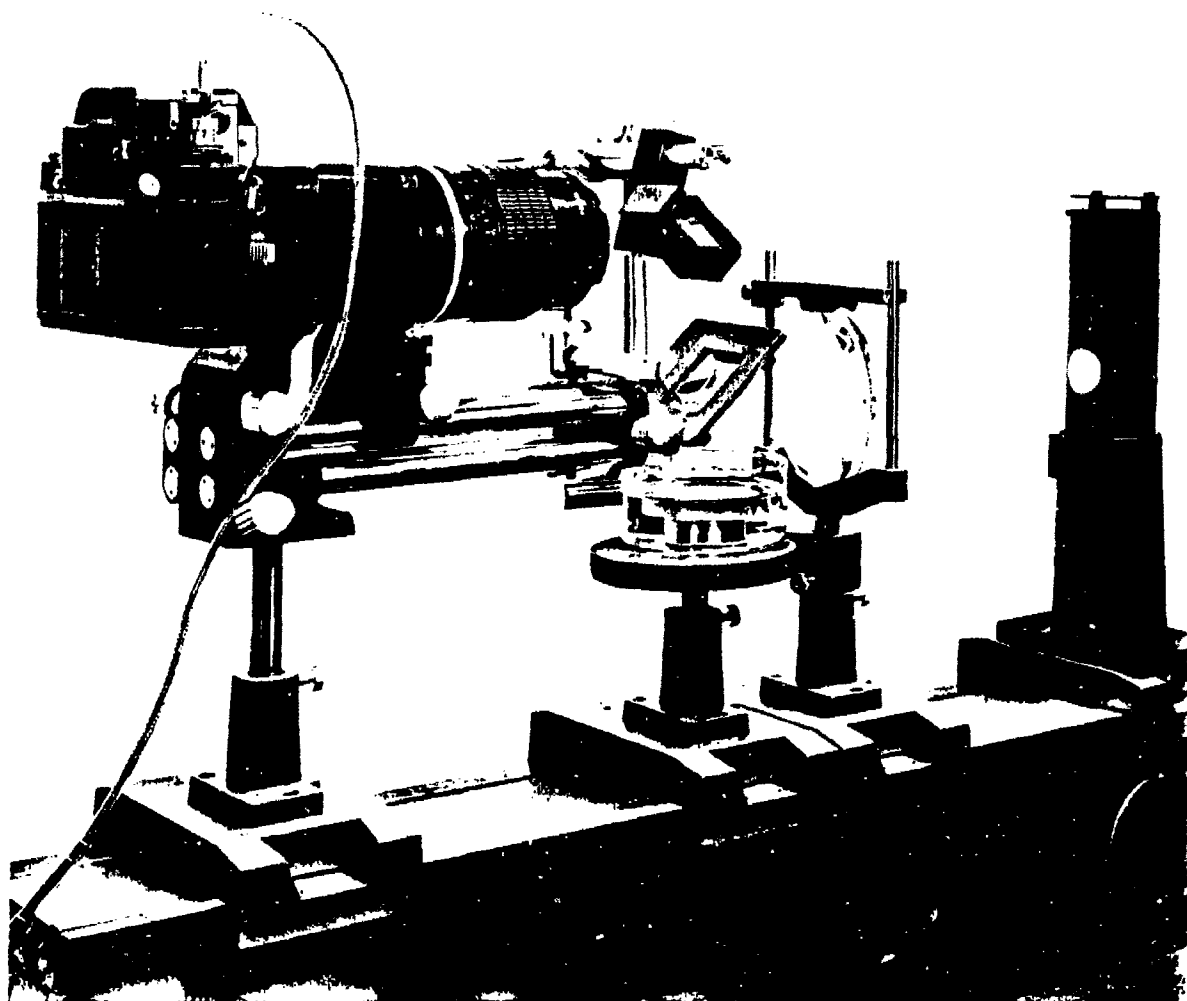
Figure 2   General view of ambient temperature apparatus.
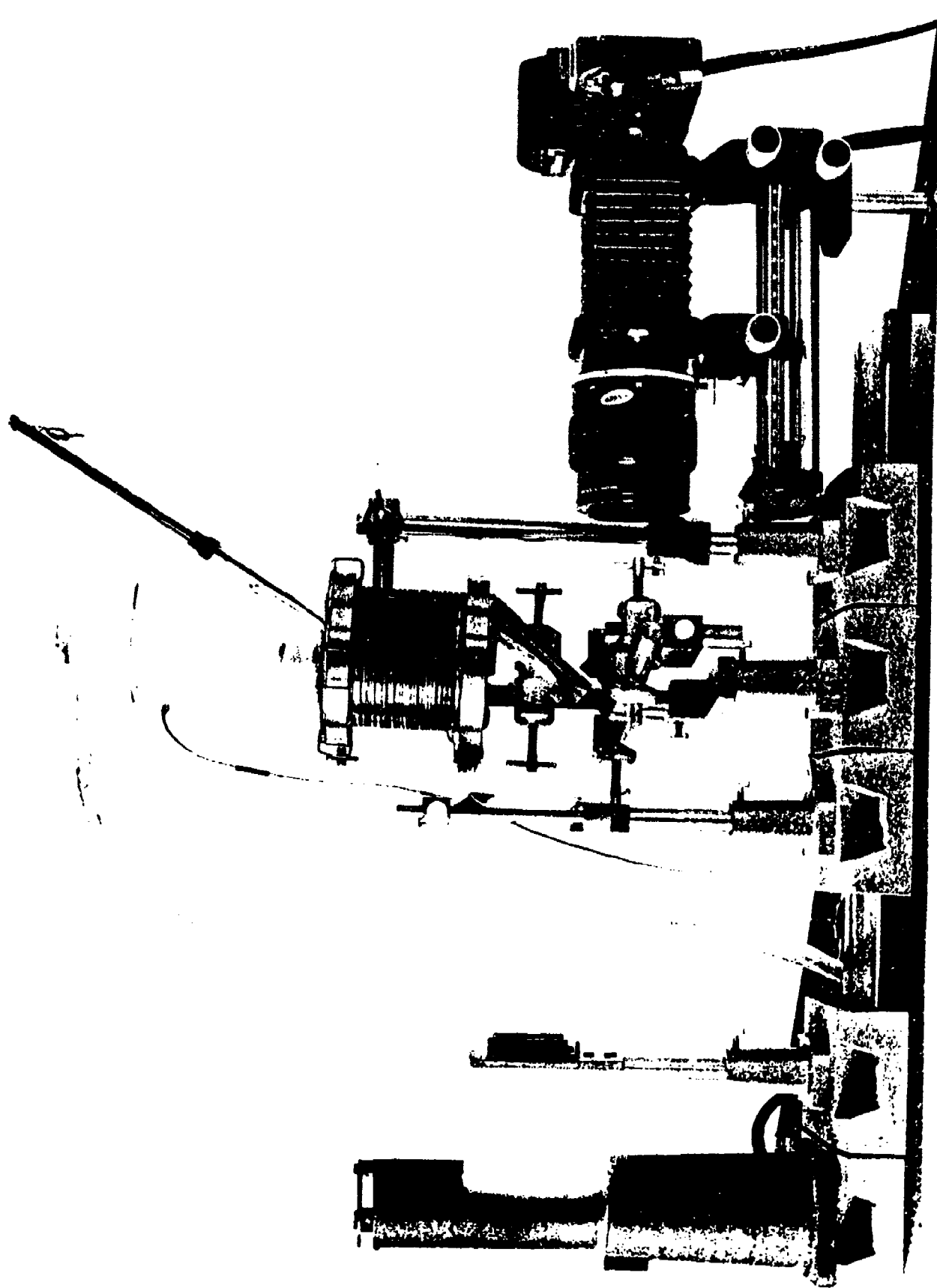
Figure 3   High temperature ($< 100^{\circ}$C) apparatus
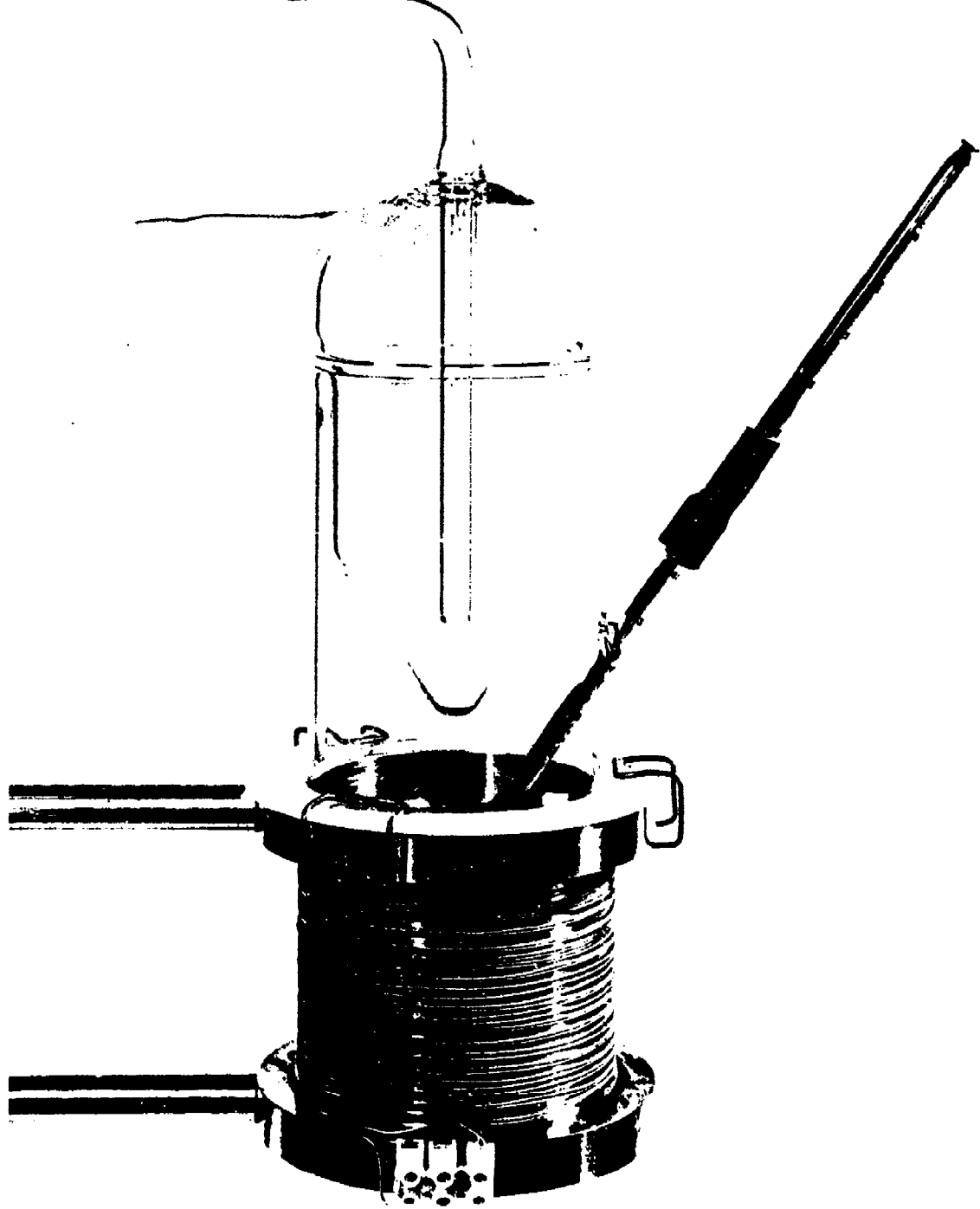
Figure 4   Mark II hot water apparatus.
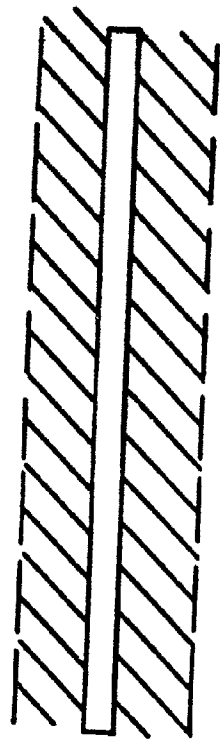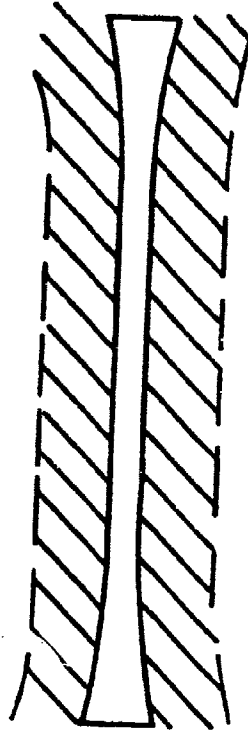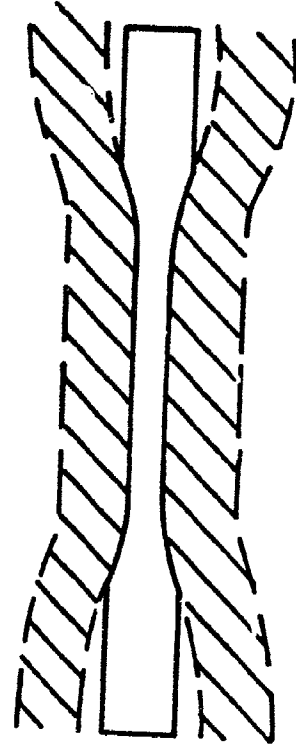
Figure 5   Inhomogeneous swelling associated with water uptake
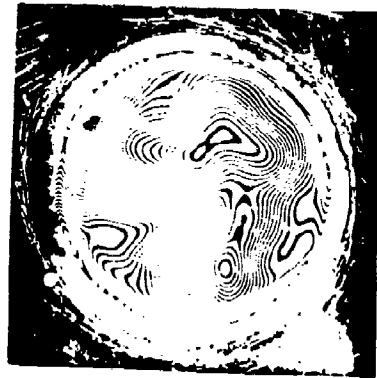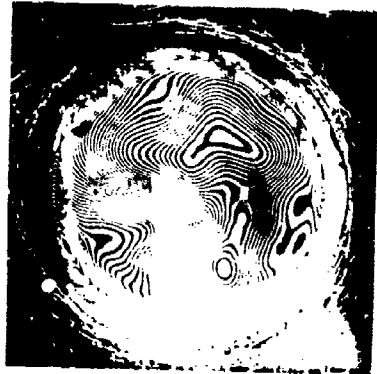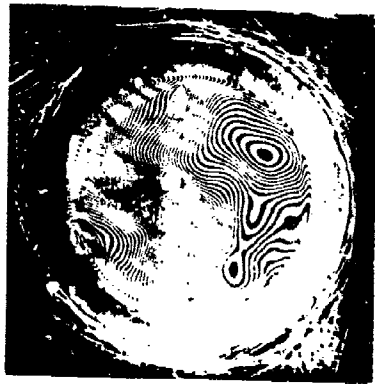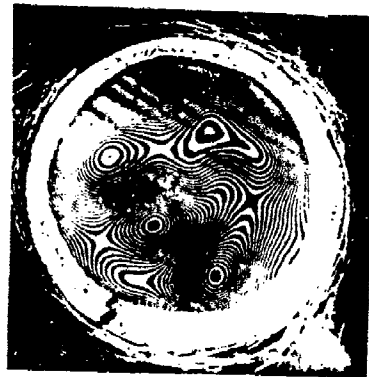
Figure 6   Sequence of interference patterns showing the swelling and debonding of FM 1000 epoxy resin film adhesive during immersion in water at 80°C.

6 hrs

192 hrs

2 hrs

76 hrs

1/2 hr

23 hrs
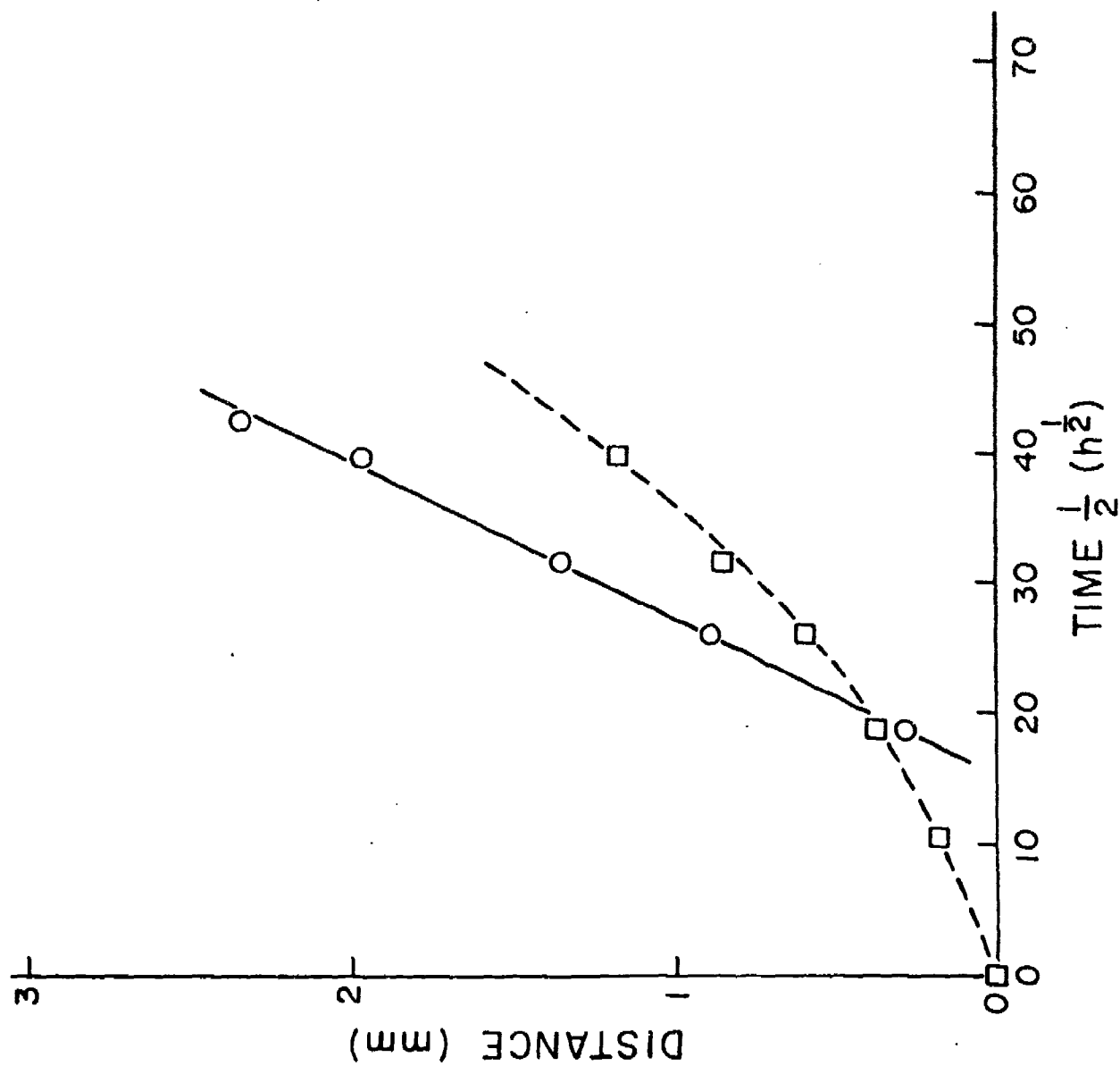
Figure 7   Migration of the shoulder in a *Newton's* ring (□) and of a point on the debonding crack (○). 20° water.
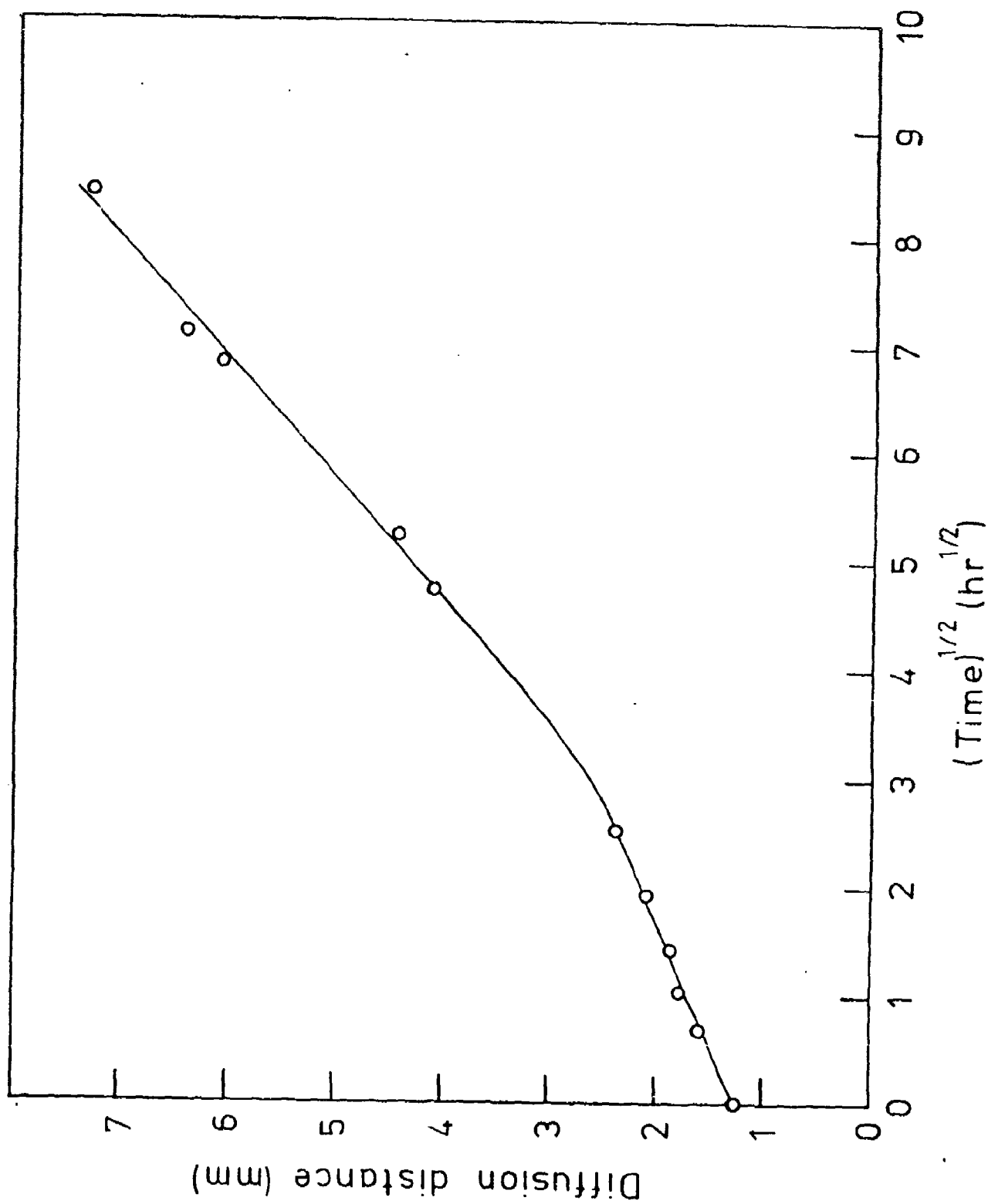
Figure 8   Diffusion rate for an FM 1000 adhesive joint between anodized titanium and glass cover slip.

STAINLESS STEEL   FM 1000   ~80° C

Diffusion distance   mm

— (Time)½ – 6 —→ hr½

Debonding starts
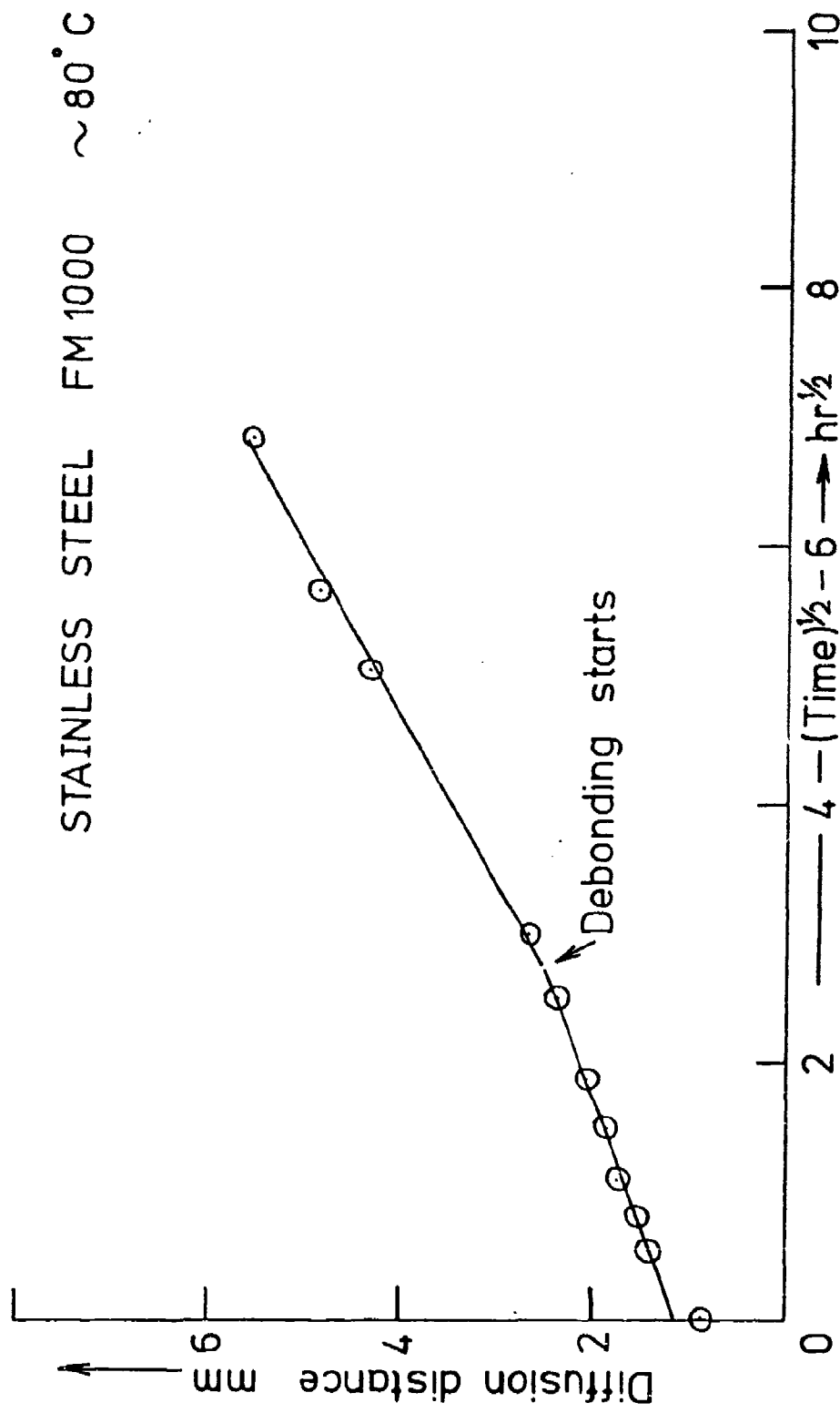
Figure 9.   Diffusion rate for an FM 1000 adhesive joint between
stainless steel and glass cover slip
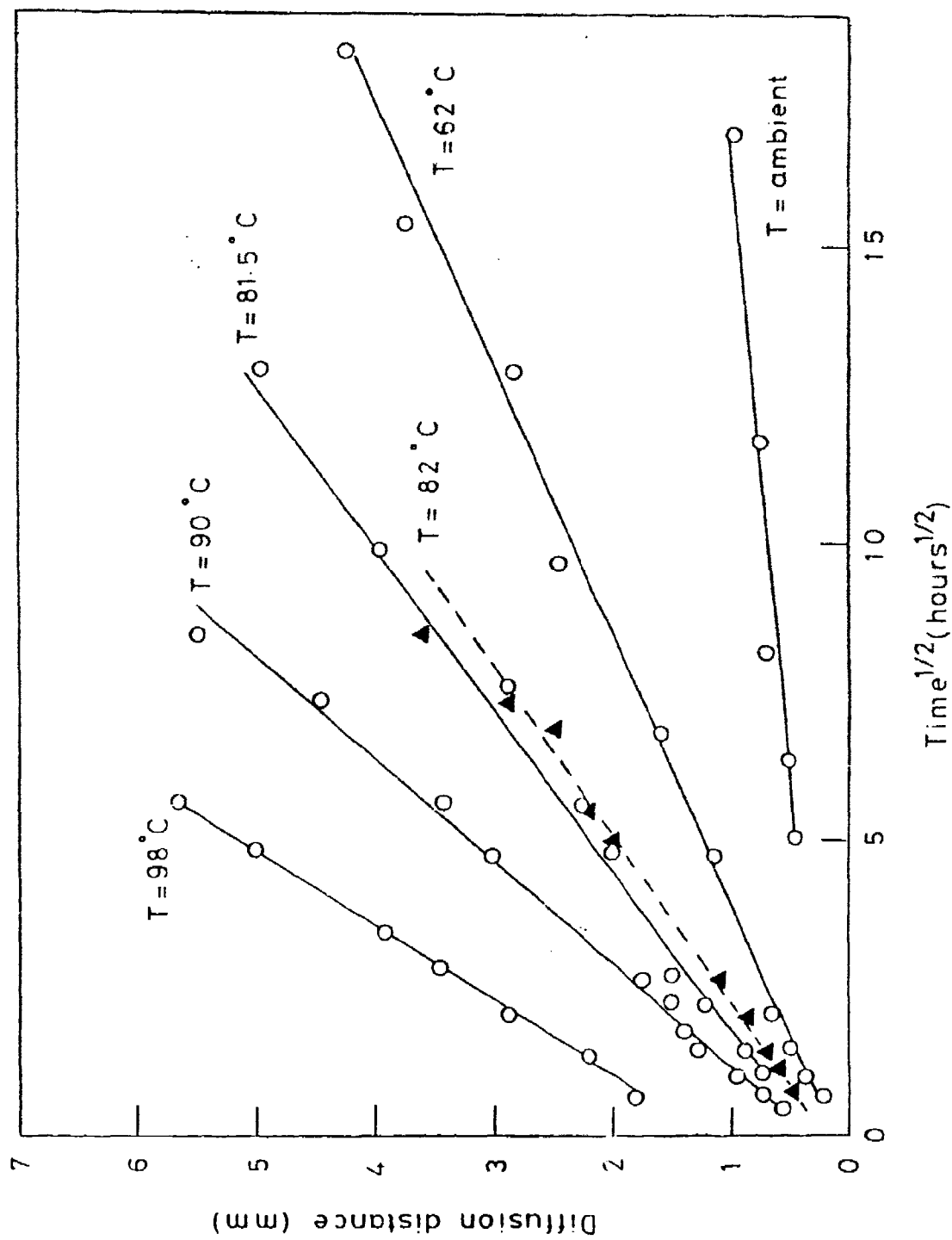
Figure 10   Migration distance of the 1st Moiré fringe for Redux 312/5   O,
and FM 73M ▲   , against the square root of time.

Figure 11   Plot of $\ell_{IC}/(\ell_{IC})_{max}$ - specimen A.

Immersion time —— mins ——

$\dfrac{\ell_{IC}}{[\ell_{IC}]_{max}}$

1·0

0·5

0

125   130   135   140
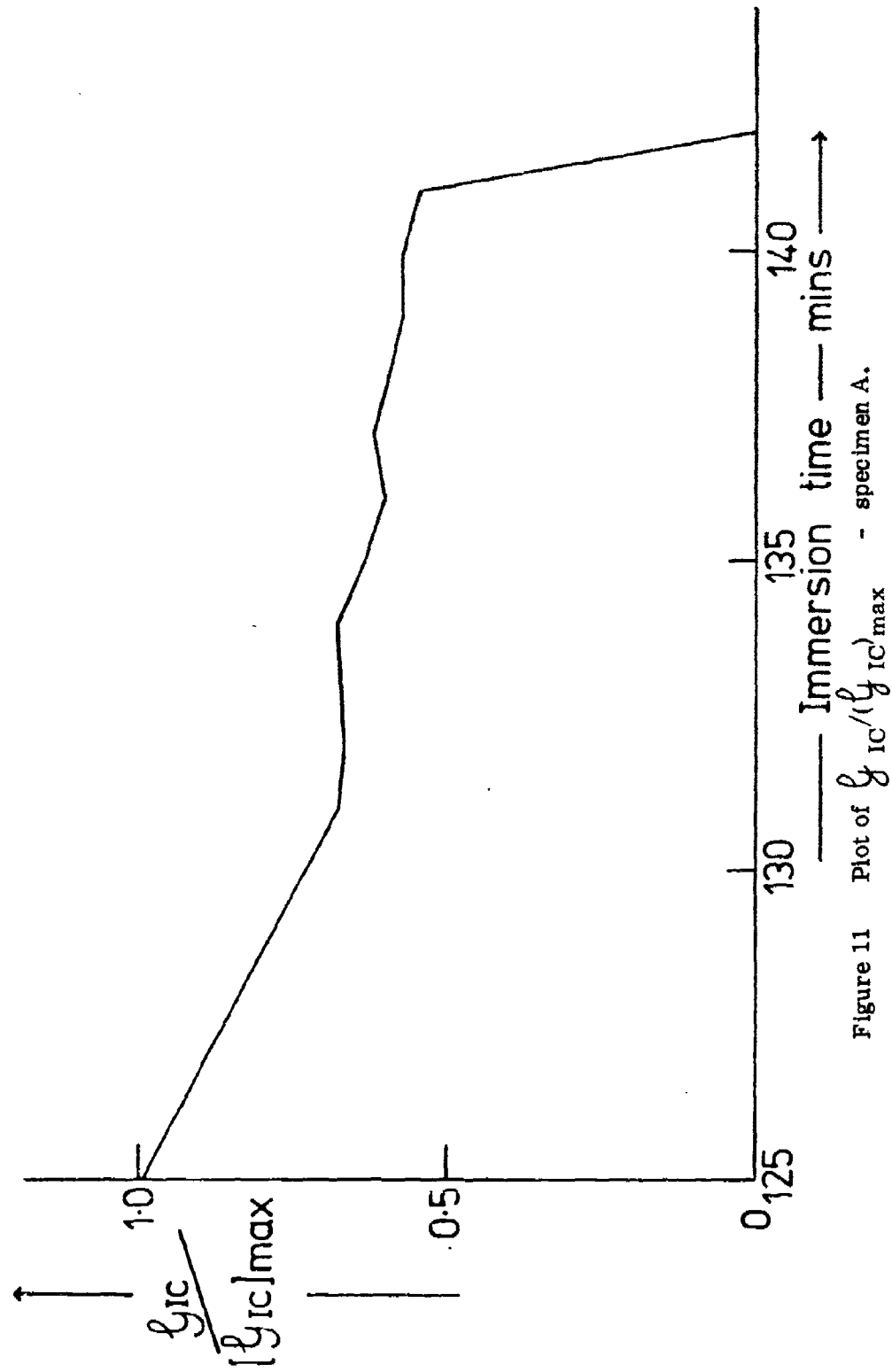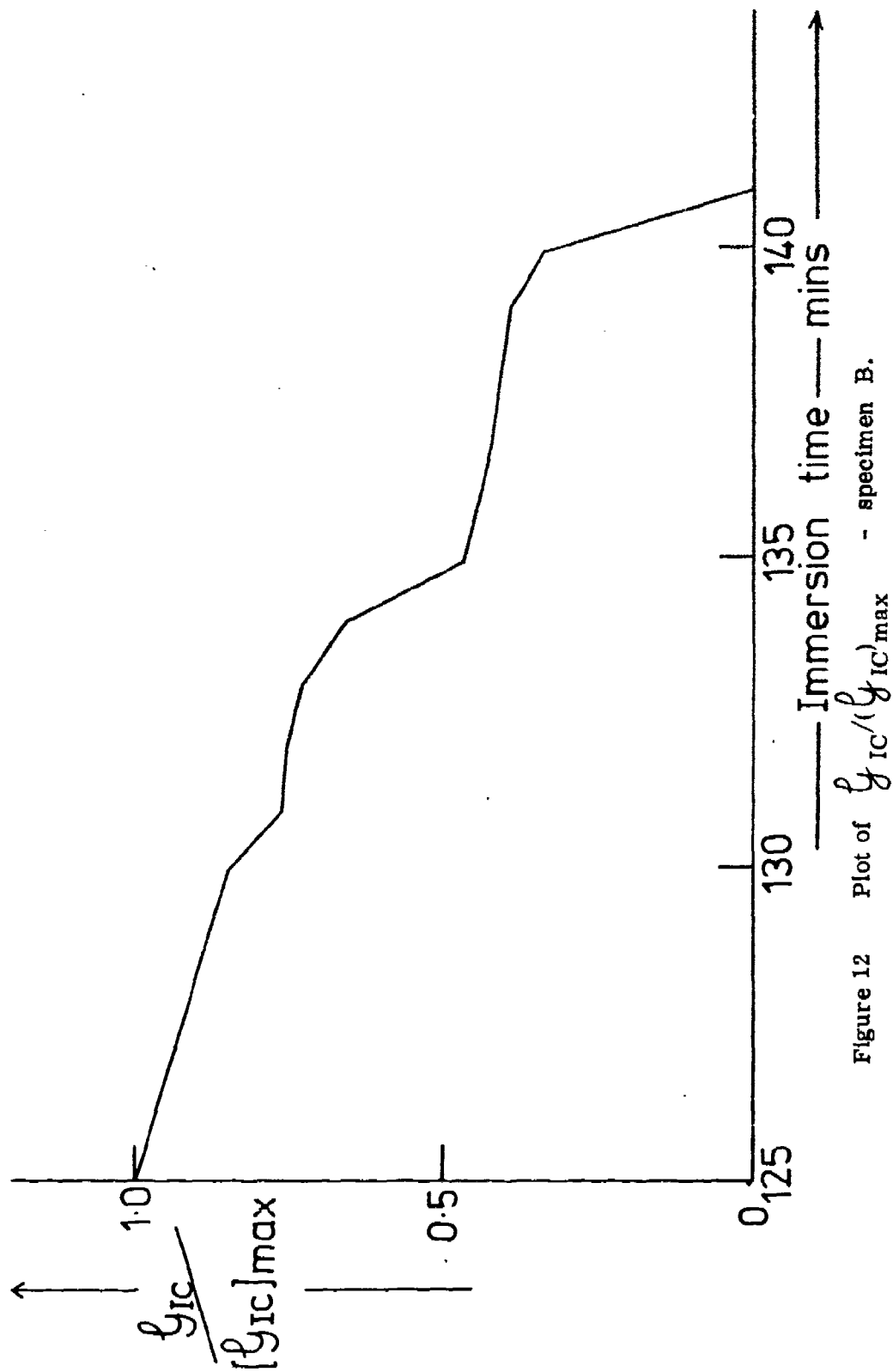
Figure 12   Plot of $\ell_{y_{IC}}/(\ell_{y_{IC}})_{max}$ - specimen B.
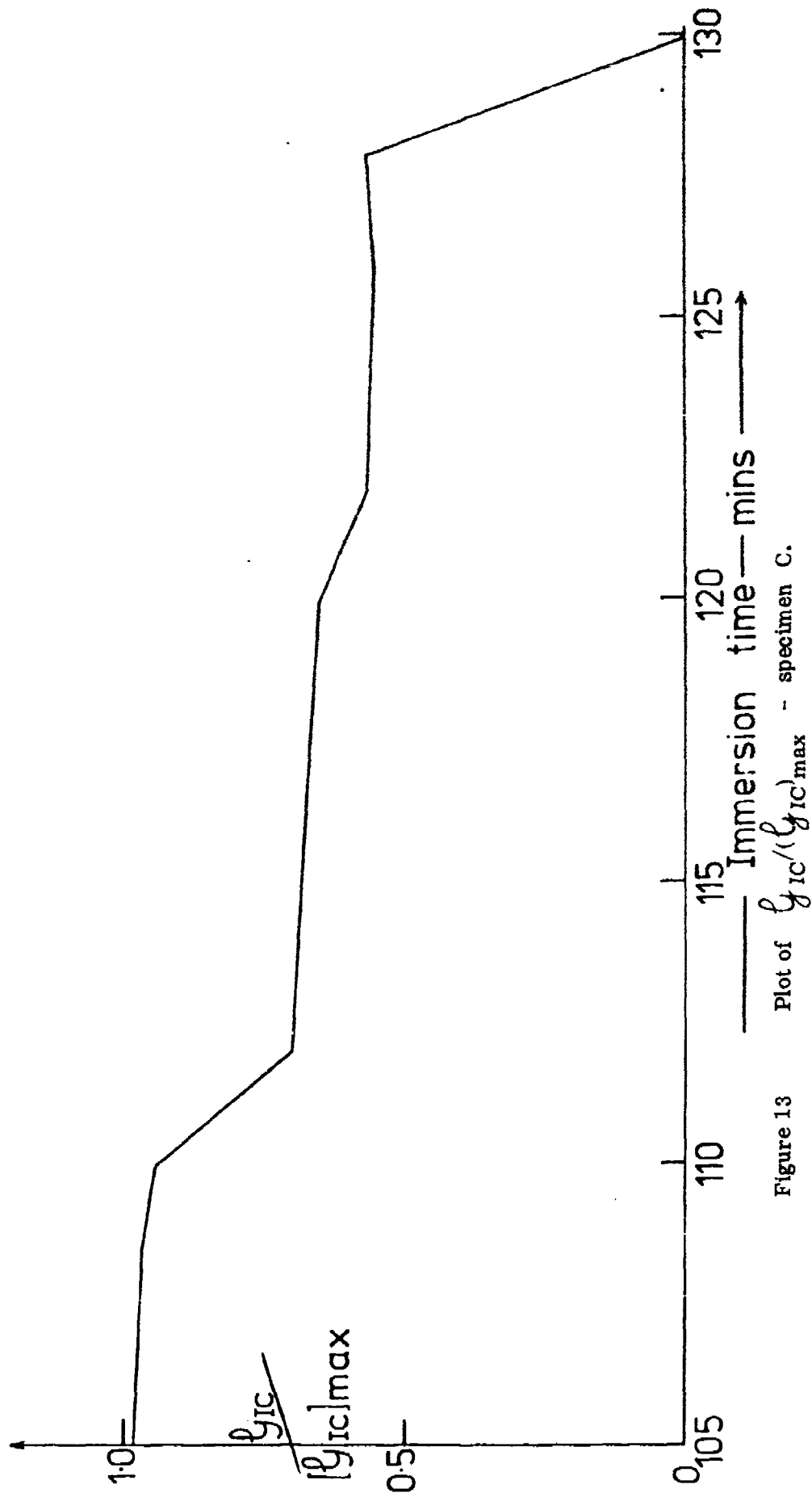
Figure 13   Plot of $\ell_{y_{IC}}/(\ell_{y_{IC}})_{max}$ - specimen C.
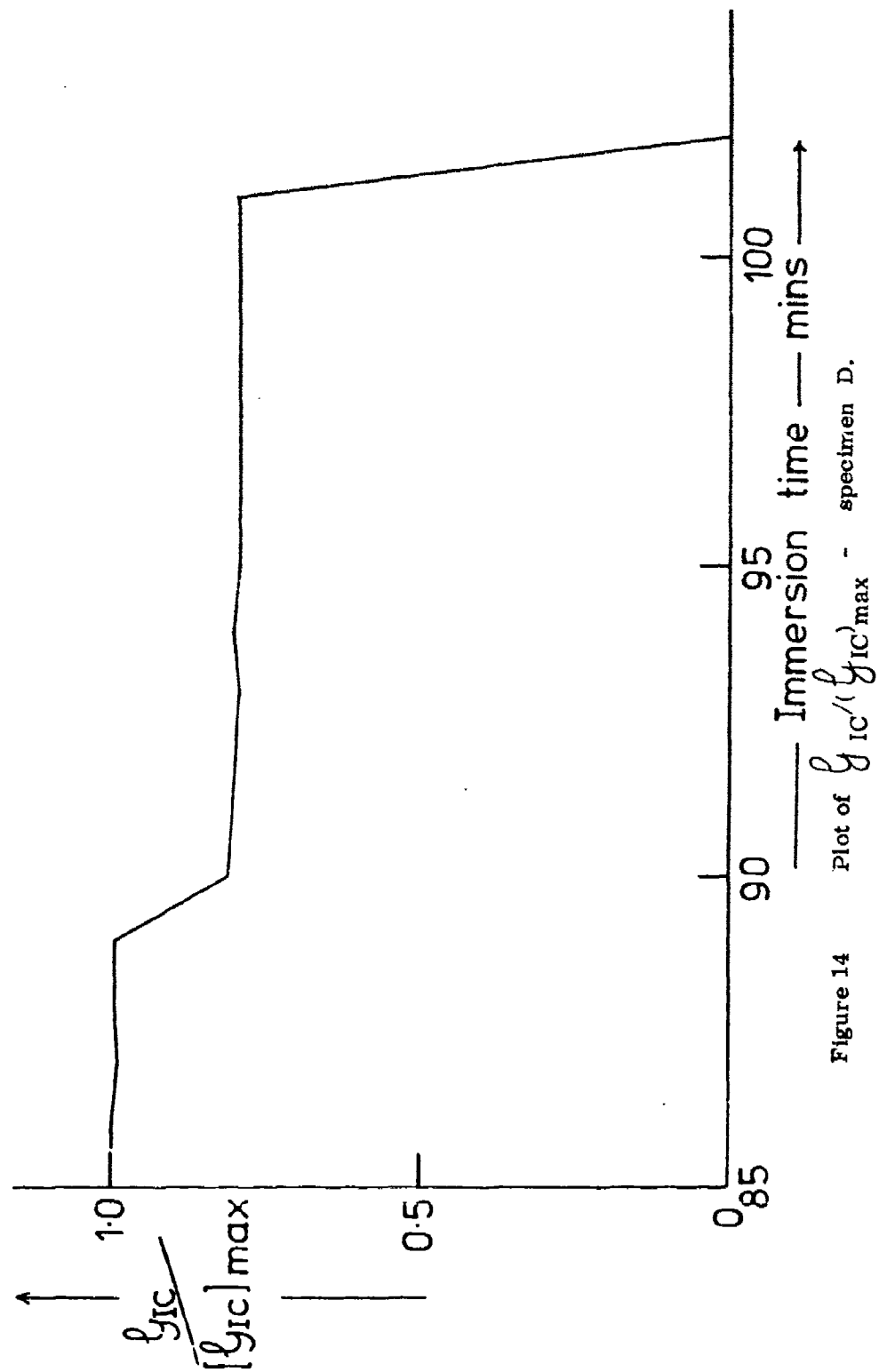
Figure 14   Plot of $\ell_{\mathcal{J}IC}/(\ell_{\mathcal{J}IC})_{max}$ - specimen D.
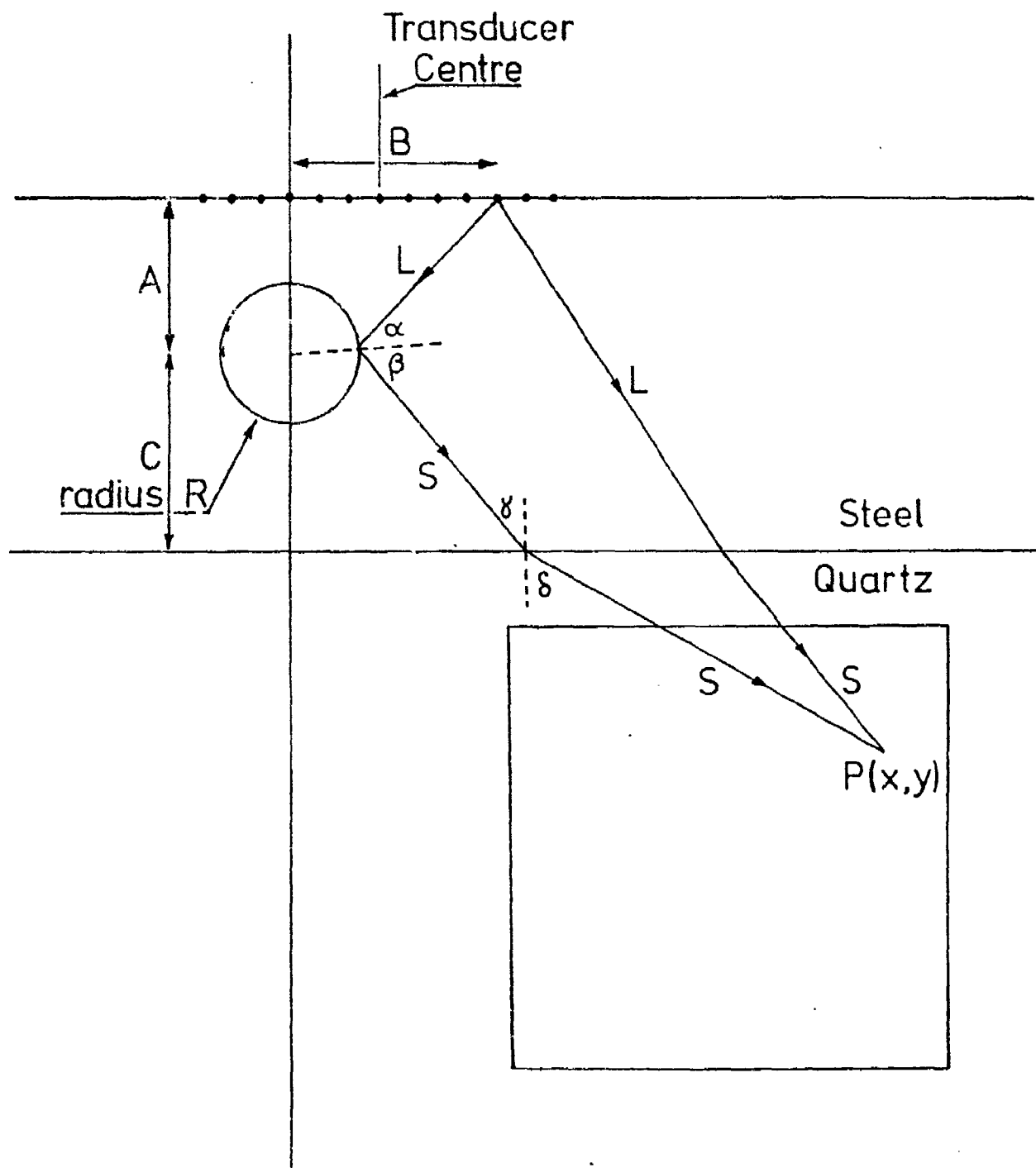
Figure 15

Computer model Representation
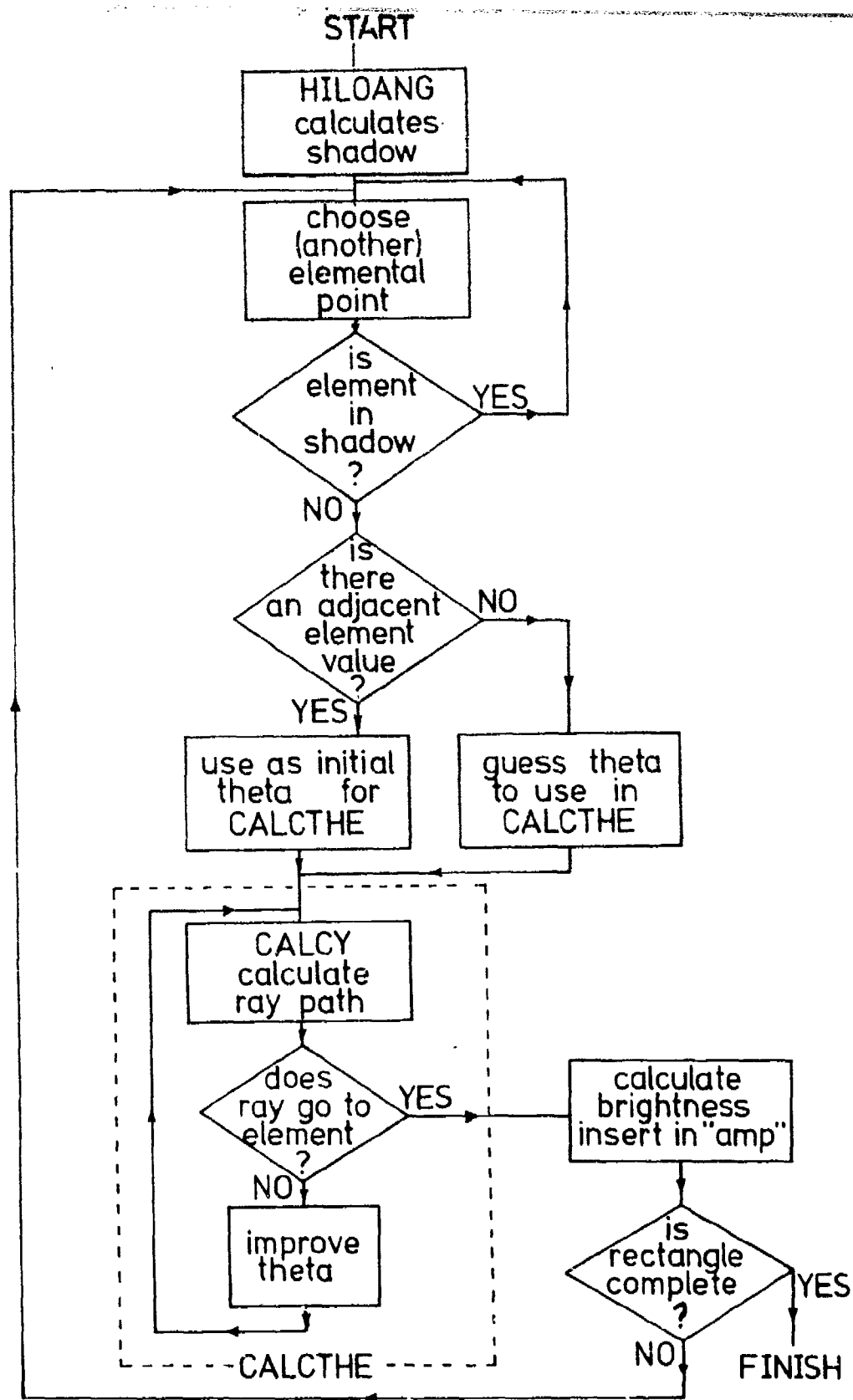
Figure 16   Flow diagram of program REFPATH.
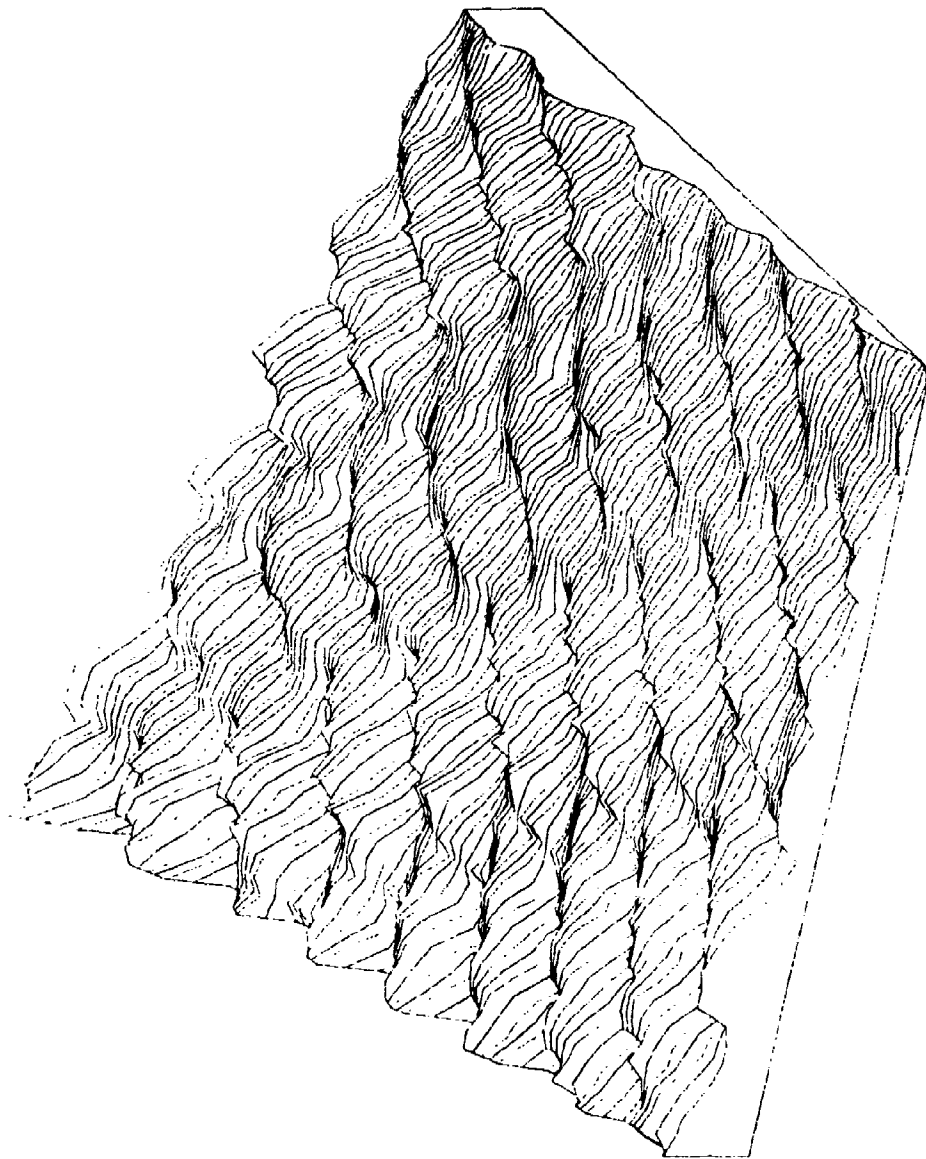
Figure 17   SYMVU representation for steel specimen with 1 mm radius hole.
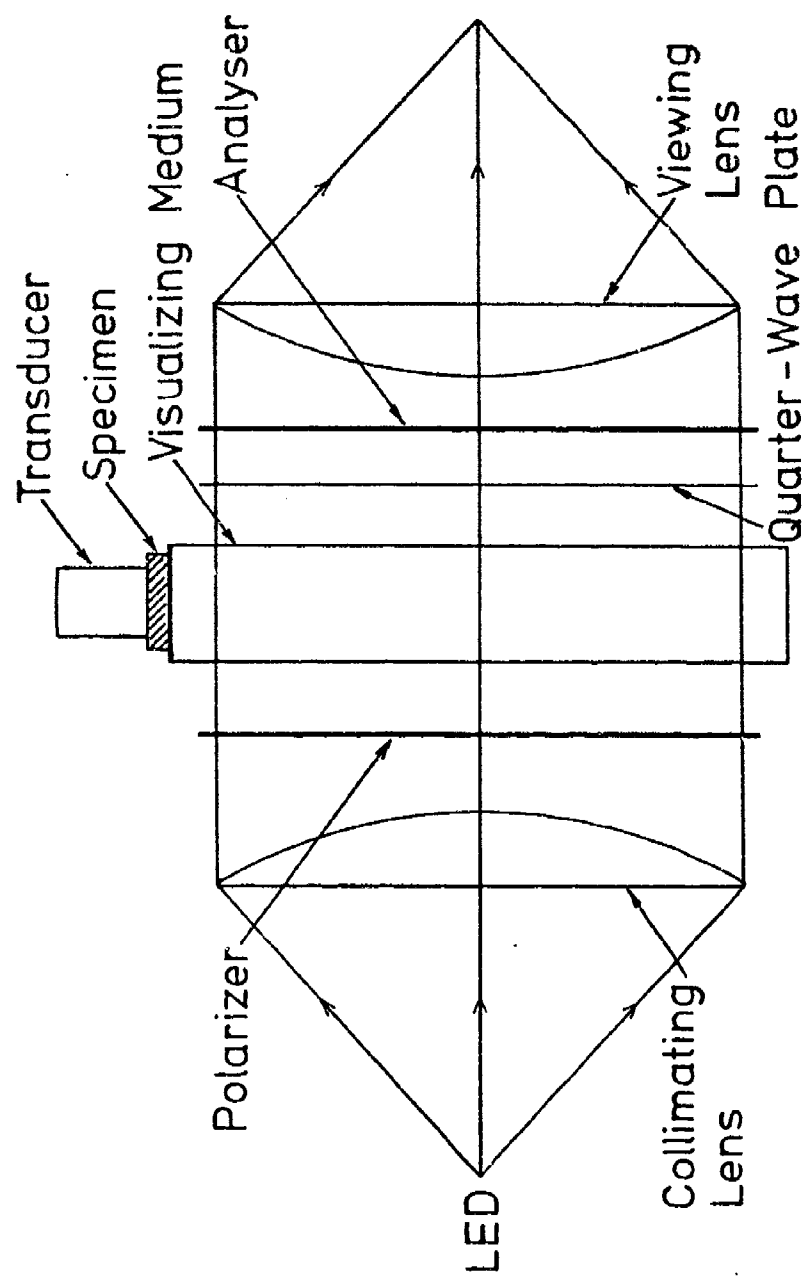
Figure 18   Schematic diagram of photoelastic system.
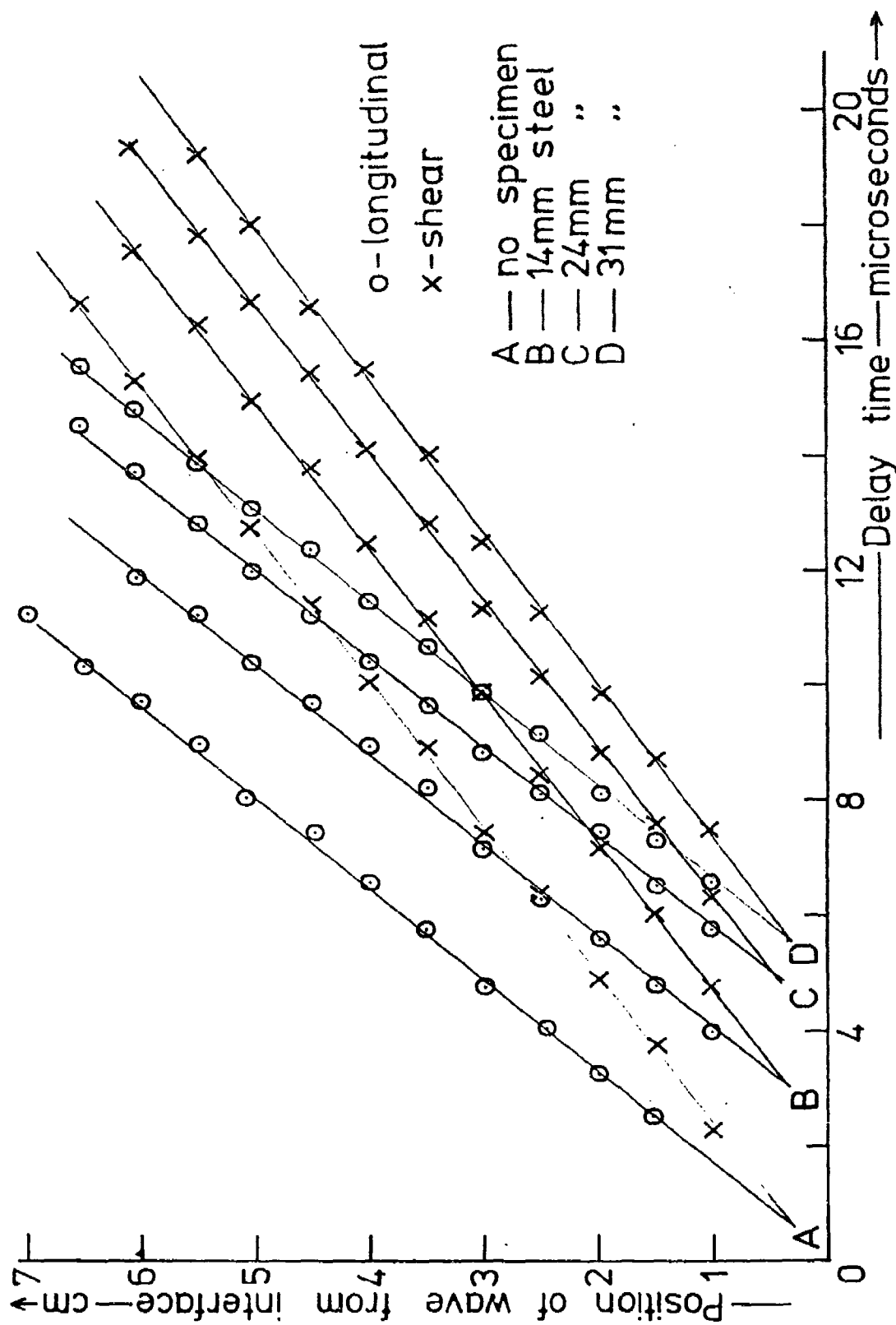
Figure 19   Position of longitudinal and shear wavefronts vs. delay.

3 × 3 cm

$(x,y) = (1.50, 2.00)$ cm
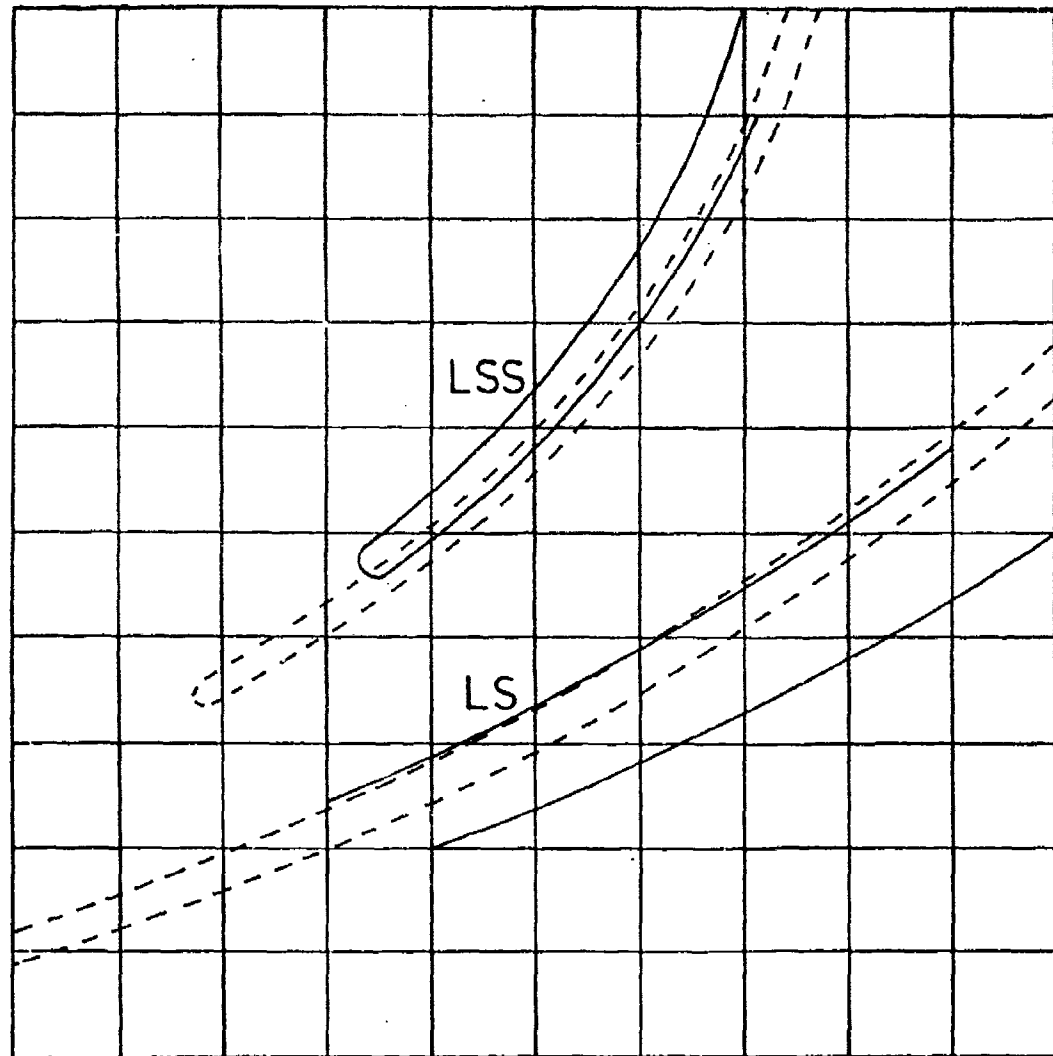
—— Photograph   ----- Computer prediction
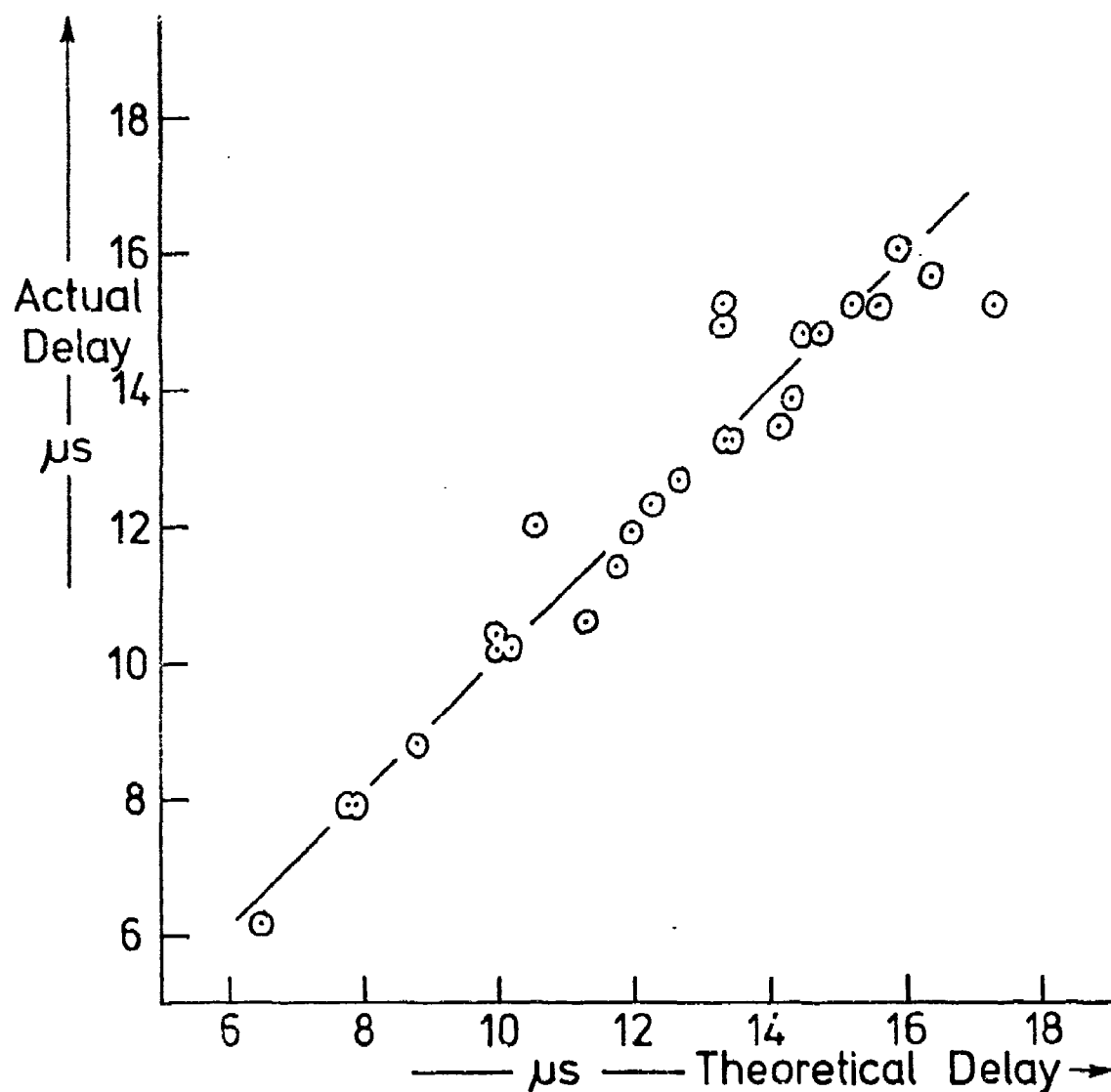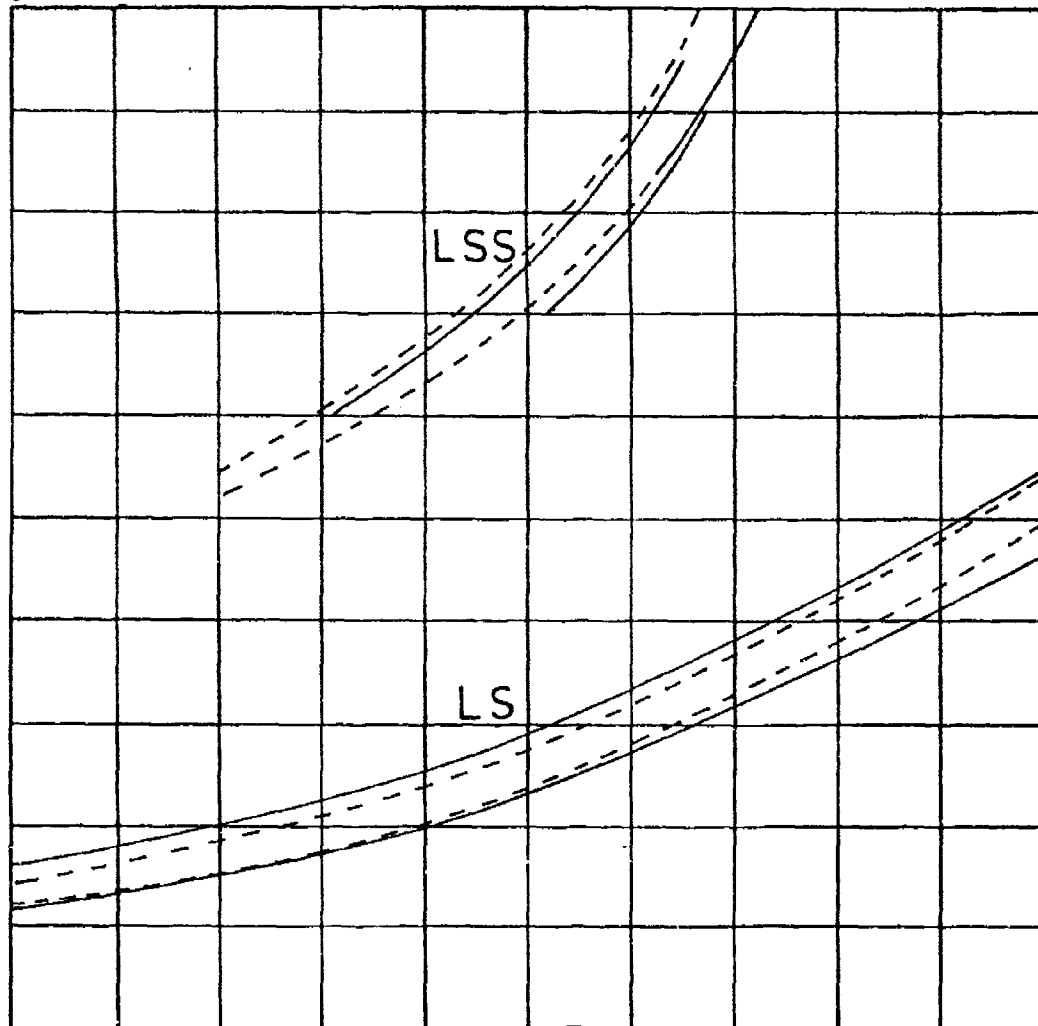
Photograph-Printout Comparison

Delay = 8.8 μs
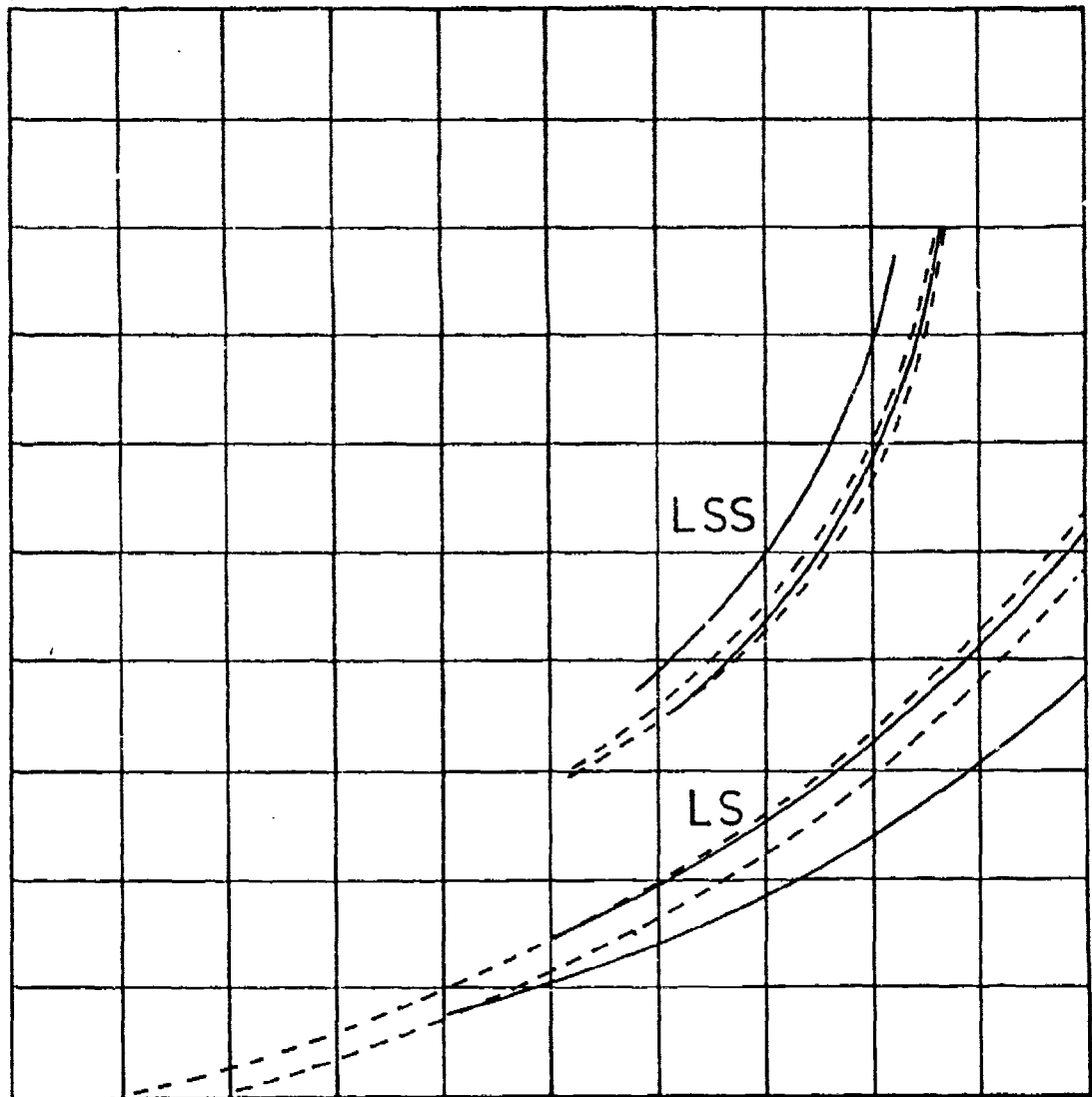
Figure 20   Computer Simulation

3×3 cm

$(x,y) = (1.50, 2.00)$ cm

———— Photograph   − − − − − Computer prediction

Photograph−Printout Comparison

Delay = 13.4 μs

Figure 21   Computer simulation

Figure 22

Experimental vs. theoretical delays

$$4 \times 4 \, cm$$

$(x,y) = (3.92, 2.00) \, cm$

LSS

LS

———— Photograph   ----- Computer prediction

Photograph-Printout Comparison

$$A = 7.0 \, mm$$

Figure 23   Computer simulation
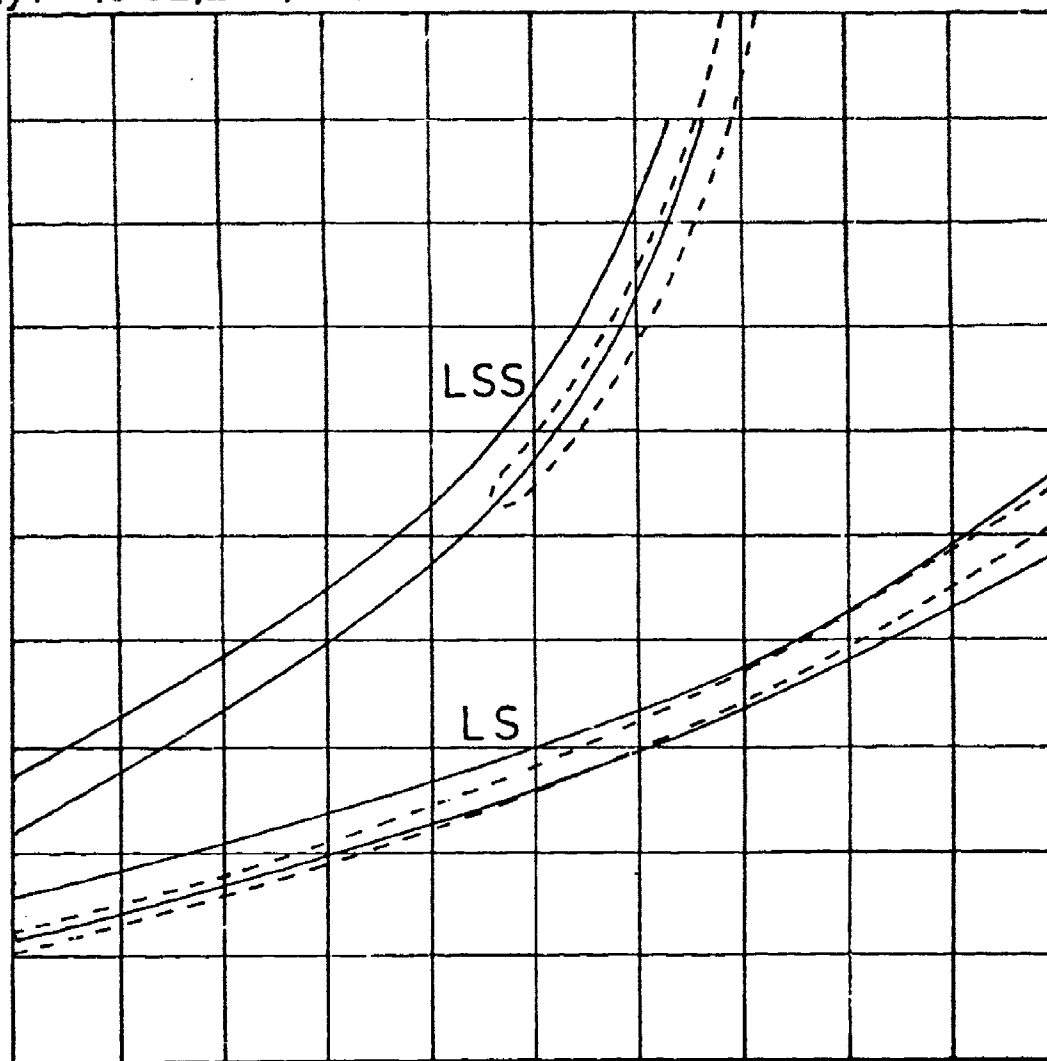
4 × 4 cm

(x, y) = (3·92, 2·00) cm

LSS

LS
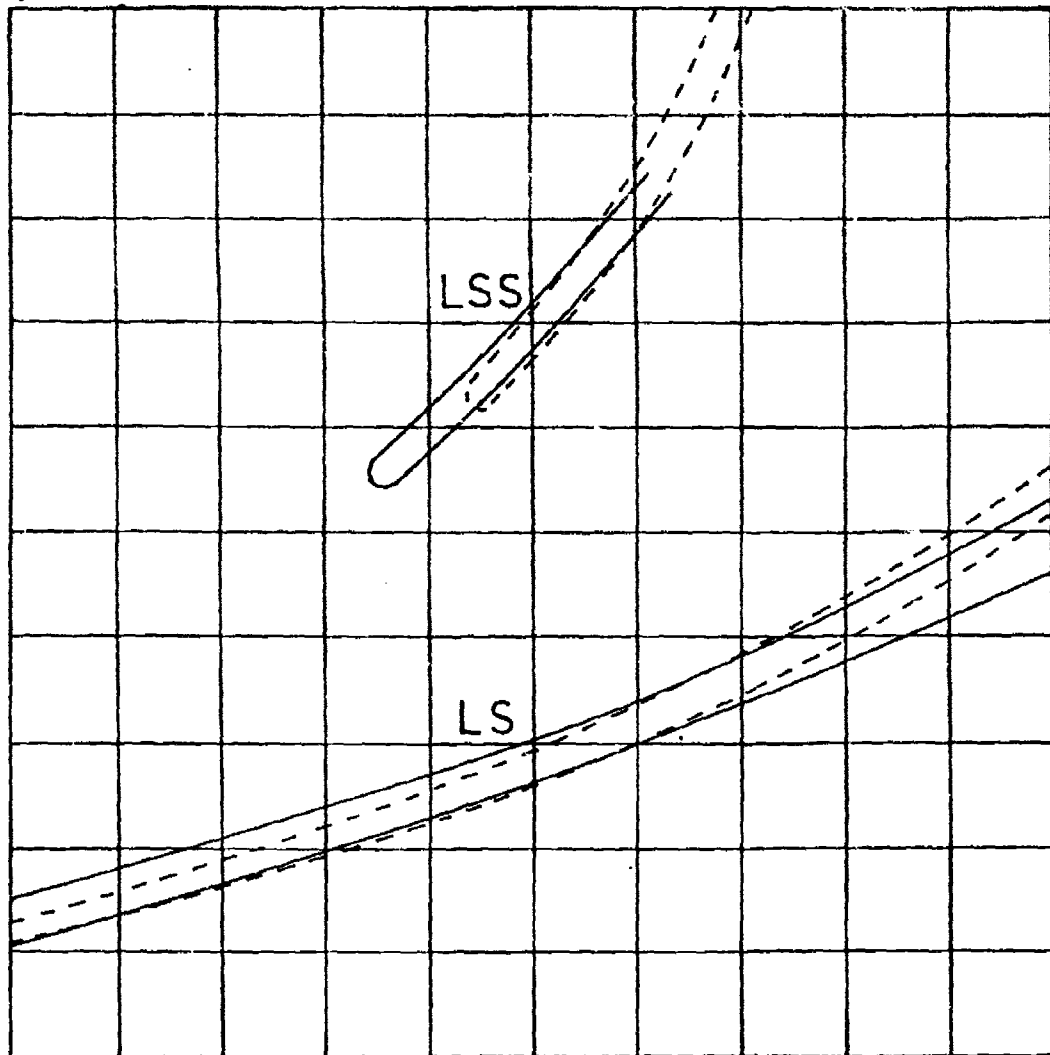
——— Photograph   ------ Computer prediction

Photograph–Printout Comparison

A = 15·6 mm

Figure 24   Computer simulation

4 × 4 cm

(x,y) = (3·92, 2·00) cm

LSS

LS

——— Photograph   - - - - - Computer prediction

Photograph-Printout Comparison

A = 24·2 mm

Figure 25   Computer simulation

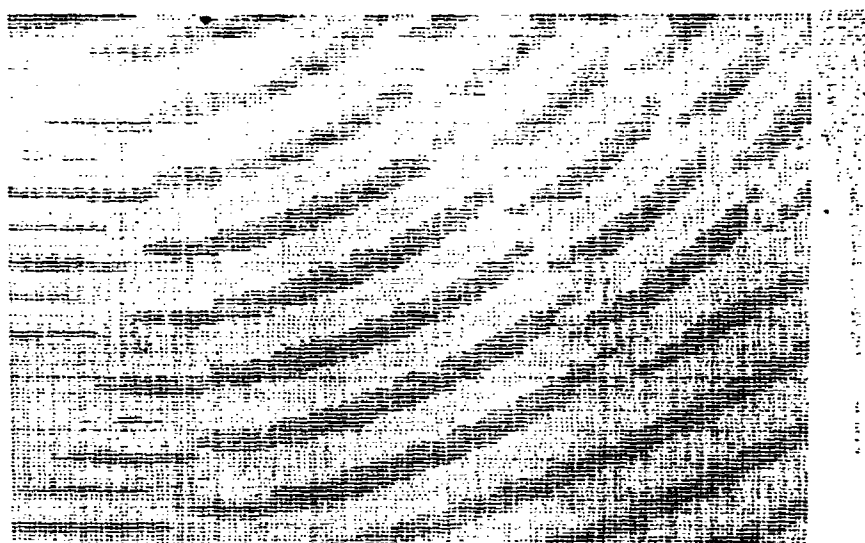Figure 26   Interference pattern from reflected shear wave (LSS) from a 1 mm radius hole in steel (multiflash).

Figure 27   Computer simulation of Figure 26.